

ORIGINAL ARTICLE OPEN ACCESS

Confronting Episodic vs. Continuous Heat Sources in Long-Lived Hot Orogens: Insights From Petrochronological Studies in the Nova Venecia Complex, Araçuaí Orogen (SE Brazil)

Lucas R. Schiavetti¹  | Vinicius T. Meira¹  | Sean Mulcahy² | Jeffrey D. Vervoort³ | Peter L. Baker³ | George L. Luvizotto⁴ | Ricardo I. F. Trindade⁵

¹Departamento de Geologia e Recursos Naturais, Instituto de Geociências, Universidade Estadual de Campinas, Campinas, Brazil | ²College of Science and Engineering, Geology Department, Western Washington University, Bellingham, Washington, USA | ³School of the Environment, Washington State University, Pullman, Washington, USA | ⁴Departamento de Geologia, Instituto de Geociências e Ciências Exatas, Universidade Estadual de São Paulo, Rio Claro, Brazil | ⁵Geofísica e Ciências Atmosféricas, Departamento de Geofísica, Instituto de Astronomia, Universidade de São Paulo, São Paulo, Brazil

Correspondence: Lucas R. Schiavetti (lucas_geologia@hotmail.com) | Vinicius T. Meira (vtmeira@unicamp.br)

Received: 20 November 2024 | **Revised:** 14 July 2025 | **Accepted:** 30 July 2025

Funding: This work was supported by Fundação de Amparo à Pesquisa do Estado de São Paulo (2016/06114-6, 2017/003528-8, 2018/06011-8, 2021/00967-5) and Conselho Nacional de Desenvolvimento Científico e Tecnológico (314473/2021-1).

Keywords: Brasiliano orogeny | garnet dating | long-lived orogeny | thermodynamic modelling | West Gondwana | zircon dating

ABSTRACT

Orogenic belts that sustain elevated temperatures at intermediate crustal depths for tens of millions of years are known as hot orogens. The evolution of these hot orogens is largely influenced by thermal maturation, primarily driven by the distribution of heat-producing elements (HPEs), such as K, Th and U in the overthickened crust. This process involves widespread anatexis, granulite facies metamorphism, extensive transfer of fluids and magma and large-scale crustal flow. Although most of the thermal evolution of hot orogens is controlled by HPEs, episodic heat transfer may also contribute to their geodynamic development. The Araçuaí orogen, located in southeastern Brazil, represents a Neoproterozoic hot orogen that exposes in its internal domain deeper levels of an overthickened crust, resembling the Tibetan plateau. Its evolution involves more than 120 million years of magmatism and metamorphism, including ultra-high-temperature metamorphism. Different geodynamic models have been suggested to explain the thermal evolution of this orogen, ranging from episodic heat sources within subduction-collisional orogeny to continuous long-lived heat sources in collisional or intracontinental settings. In this paper, we integrate detailed thermodynamic modelling, Lu–Hf and Sm–Nd garnet dating, and U–Pb and REE zircon data from an outcrop that includes granulite facies metasedimentary rocks (Nova Venecia complex) and an intrusive gabbroic stock (São Gabriel pluton). This key outcrop allows us to investigate the history of high-grade regional metamorphism within the internal domain of the Araçuaí orogen, as well as the thermal impact of the late-stage high-temperature magmatism on the later evolution of this hot orogen. Our data indicate that the studied rocks reached near-peak conditions (6.5–10 kbar and ~800°C) at 535–530 Ma and followed a near-isothermal decompression path to 5–6 kbar at ~530–520 Ma. Only local effects of contact metamorphism (~5 kbar and 900°C–1000°C) were observed along the contact between the gabbroic stock and its host rock. Based on this newly integrated dataset and the compilation of existing information, we argue that the Araçuaí orogen evolved from a single, continuous, long-lived heat source controlled by radiogenic decay from HPEs, rather than episodic advective heating from subduction/collision-related processes.

This is an open access article under the terms of the [Creative Commons Attribution](#) License, which permits use, distribution and reproduction in any medium, provided the original work is properly cited.

© 2025 The Author(s). *Journal of Metamorphic Geology* published by John Wiley & Sons Ltd.

1 | Introduction

Large and wide orogenic belts that maintain elevated temperatures at intermediate crustal depths (~15–35 km) for tens of millions of years are recognized as hot orogens (Ellis et al. 1998; Chardon et al. 2009; Beaumont et al. 2010). The thermal evolution of this type of orogen is largely controlled by the distribution of heat-producing elements (HPEs) in the overthickened crust (e.g., England and Thompson 1984; Bea 2012; Clark et al. 2011, 2015). Nevertheless, episodic increases in heat resulting from enhanced mantle heat flow and advective heating due to mafic and/or felsic melt emplacement may also play a role in its evolution (Collins 2002; Brown 2007; Clark et al. 2014; Farias et al. 2023, among others). These episodic heating events can be attributed to diverse geodynamic processes such as slab retreat, arc maturation, slab window subduction, slab breakoff and back-arc extension (Jiao et al. 2023 and references therein). Indeed, the range of geodynamic processes that can influence the thermal evolution of hot orogens offers numerous possibilities for interpreting their geodynamics.

Well-studied examples of collisional hot orogens, such as the Himalaya-Tibet, Grenville and Variscan orogens, highlight the complexity of their long-lived geodynamic evolution (e.g., Jamieson et al. 2004, 2010; Parsons et al. 2020; Kelly et al. 2020, 2022; Johnson et al. 2020). Petrological and geochronological data from ancient orogens, especially those from the Proterozoic era, indicate that large hot orogens remained at suprasolidus temperatures for tens to hundreds of millions of years (Montero et al. 2004; Smithies et al. 2011; Johnson et al. 2015; Clark et al. 2015; Rocha et al. 2017; Cavalcante et al. 2018; Turlin et al. 2018). Therefore, one of the most difficult questions regarding their evolution involves identifying the heat source(s) needed to keep these thickened continental crusts hot for such extended periods (Brown 2007; Clark et al. 2011; Jiao et al. 2023).

The Araçuaí orogen represents a long-lived hot orogen associated with the assembly of West Gondwana that records magmatic activity and tectonism spanning from 630 to 480 Ma (e.g., Pedrosa-Soares et al. 2001; Alkmim et al. 2006). It corresponds to the Brazilian counterpart of the Brasiliano/Pan African Araçuaí-West Congo orogen, which is characterized by a confined geometry in a continental gulf between the São Francisco and Congo cratons (e.g., Alkmim et al. 2006, Figure 1a,b). The complex geological record and the confined geometry of the orogen stimulate an active discussion regarding its tectonic model and geodynamic evolution (e.g., Fossen et al. 2020). The models that include oceanic plate consumption with subduction and collisional tectonics are based primarily on geochemical, isotopic and geochronological data of orthogneisses and granitoids (e.g., Pedrosa-Soares et al. 2011; Tedeschi et al. 2016), and metamafic-ultramafic rocks interpreted as fragmented ophiolites within an accretionary wedge (Pedrosa-Soares et al. 1998; Peixoto et al. 2015; Amaral et al. 2020). These tectonic models typically incorporate episodic heat sources to account for the protracted evolution of the Araçuaí orogen, such as mid-ocean ridge subduction, slab retreat, slab break-off and back-arc extension (e.g., Gradim et al. 2014; Bento dos Santos et al. 2015; Tedeschi et al. 2016;

Richter et al. 2016). On the other hand, tectonic models that link the evolution of the Araçuaí orogen with either a plateau-like intracontinental orogeny (e.g., Cavalcante et al. 2019, 2021; Fossen et al. 2020) or crustal overthickening with limited oceanic consumption (Fossen et al. 2017; Schannor et al. 2021) highlight the importance of HPE distribution within the orogenic crust in controlling its thermal evolution. Although the tectonic model and geodynamic evolution of the Araçuaí orogen remain topics of ongoing debate, the available petrological and geochronological data, particularly those using an integrated petrochronological approach (Engi et al. 2017), offer significant insights into the thermal evolution of the orogen (e.g., Schannor et al. 2021).

In this study, we combine field data, detailed thermodynamic modelling, U-Pb and REE zircon data, as well as Lu-Hf and Sm-Nd garnet geochronology from high-grade metamorphic rocks within the internal domain, more specifically in the hot anatetic domain, of the Araçuaí Orogen in order to constrain its metamorphic evolution. This synthesis of data, along with the compilation of available P-T-t data for the Araçuaí Orogen, enables us to discuss its long-lived thermal evolution and evaluate various geodynamic hypotheses regarding the heat budget within this orogenic system.

2 | Geological Background

The Araçuaí orogen represents the Brazilian counterpart of the Araçuaí-West Congo orogen, which became separated from the African side due to the opening of the Atlantic Ocean during the Cretaceous period (e.g., Pedrosa-Soares et al. 1998, 2001). Its formation is intricately linked with the breakup of the Rodinia supercontinent and the assembly of West Gondwana during the Neoproterozoic Brasiliano/Pan-African tectonic cycle, ultimately leading to the consolidation of the South American platform (Almeida 1967). Throughout this tectonic cycle, various sedimentary basins formed, and continents fragmented before being juxtaposed during diachronic orogenic events (Brito-Neves and Cordani 1991; Brito-Neves et al. 1999; Campos Neto 2000; Alkmim et al. 2001; Heilbron et al. 2004; Fuck et al. 2008). The Araçuaí orogen is bounded by the São Francisco craton to the north and west, and the Atlantic coast to the east (Figure 1b). Its southern limit with the coeval Ribeira Orogen, also associated with the Brasiliano/Pan-African cycle, is traditionally placed at the 21°S parallel based on significant structural differences. However, regional studies indicate a gradual transition between these orogenic systems, with the Araçuaí orogen characterized by a dominant shortening regime and orogen-orthogonal crustal flow, while in the Ribeira Orogen, a transpressive regime and orogen-parallel kinematics dominate (Vauchez et al. 1994; Egydio-Silva et al. 2018).

The Araçuaí orogen can be subdivided into the external fold-and-thrust belt, in the western and northern segments, and an internal (hot) domain in its central and eastern areas (Fossen et al. 2017; Cavalcante et al. 2019, Figure 1b). The external fold-and-thrust belt exhibits very low- to medium-grade metasedimentary rocks and variably reworked basement rocks, with metamorphic conditions increasing from west to east, up to amphibolite facies (Cavalcante et al. 2019). Mylonitic

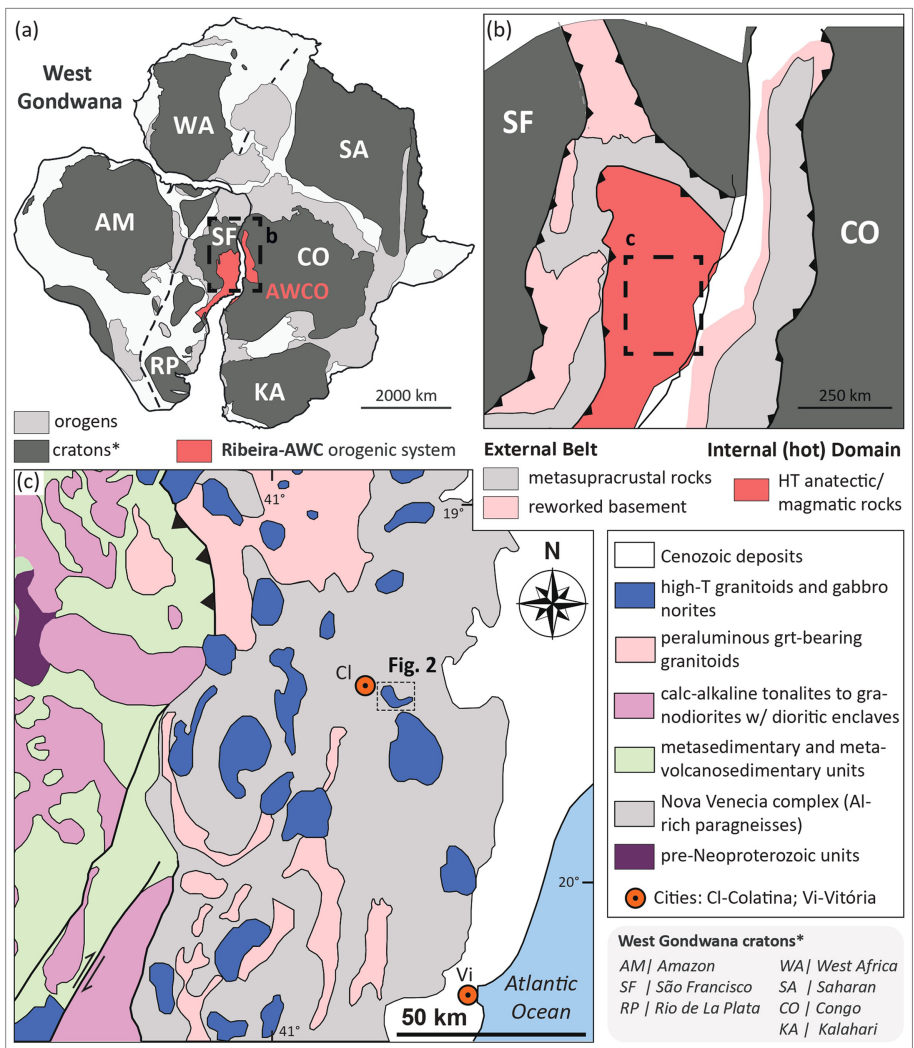


FIGURE 1 | Tectonic and geological maps of West Gondwana and Araçuaí-West Congo orogen. (a) Tectonic map of West Gondwana showing the distribution of cratonic blocks and Neoproterozoic orogenic belts around 420 Ma; (b) general tectonic map of the Araçuaí-West Congo orogen (AWCO) and surroundings, after Fossen et al. (2017); (c) simplified geological map of the eastern part of the internal (hot) domain of the Araçuaí orogen, after Melo et al. (2017b).

metasedimentary rocks forming a subhorizontal shear zone that exceeds 5 km in thickness, deformed at high temperature (~750°C), define the boundary between the external and internal domains (Vauchez et al. 2007).

The internal domain includes large tonalitic/granodioritic batholiths and medium- to high-grade metavolcanosedimentary sequences in the central domain of the Araçuaí orogen (Central Plutonic domain of Mondou et al. 2012), and voluminous peraluminous granites and garnet-biotite diatexites, migmatitic paragneisses and late high-temperature granitoids and gabbros in its eastern area, also known as the anatectic domain (Vauchez et al. 2007; Cavalcante et al. 2014; Schannor et al. 2021, Figure 1c). The migmatitic paragneisses of the anatectic domain are inferred to occur beneath the peraluminous granites and diatexites in the easternmost region of the Araçuaí orogen (e.g., Gradim et al. 2014; Melo et al. 2017b). The Nova Venecia complex is the southern exposure of the migmatitic paragneiss unit and includes mostly upper amphibolite to granulite facies metasedimentary rocks, represented by migmatitic gneisses

with variable amounts of garnet, cordierite, biotite and sillimanite; Al-rich granulites, stromatic metatexites, minor calcsilicate rocks and diatexites and peraluminous granites (Gradim et al. 2014; Richter et al. 2016).

2.1 | Nova Venecia Complex

The main lithologies grouped as the Nova Venecia complex (NVC) include Al-rich paragneisses with evidence of partial melting, lenses of refractory calcsilicate rocks, granoblastic garnet- and cordierite-rich granulites, leucocratic veins and diatexites (Figure 2a). Two main metamorphic assemblages are observed in the paragneisses: (i) sillimanite + cordierite + garnet + biotite; and (ii) garnet + cordierite ± sillimanite ± orthopyroxene ± spinel ± biotite (Gradim et al. 2014; Richter et al. 2016). A general variation of metamorphic grade from amphibolite facies in the west to granulite facies in the east is interpreted as due to the exposure of progressively deeper crustal levels (Gradim et al. 2014).

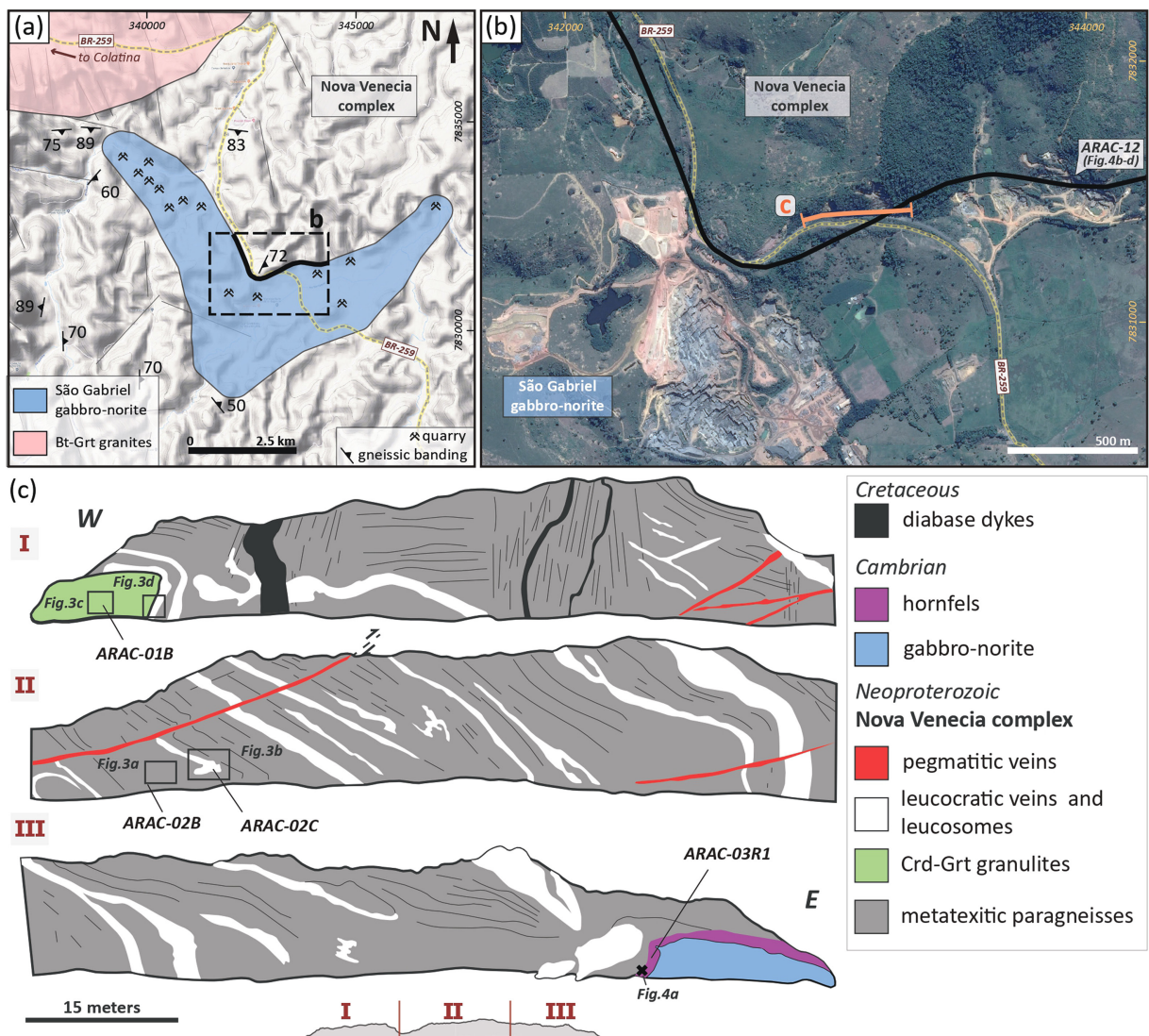


FIGURE 2 | (a) Simplified geological map near the city of Colatina, outlining the São Gabriel gabbro-norite; (b) satellite image showing the location of the studied roadcut with the indication of the contact between Nova Venecia complex and the São Gabriel gabbro-norite. Active quarries, mostly exploring the gabbro-norite for ornamental stones, are indicated, including the site ARAC-12, cited in the text; (c) schematic sketch of the studied roadcut showing field features such as leucosome parallel to the main gneissic/stromatic banding of the metatexitic paragneisses and late pegmatitic/aplithic veins crosscutting the gneissic foliation, associated with small faults. In the westernmost part of the outcrop is represented the granoblastic cordierite-garnet granulite. Cretaceous diabase dykes are also shown in the western part of the outcrop. The contact between the migmatitic paragneisses and the gabbro-norite is highlighted in the easternmost part of the outcrop.

Previous P-T estimates constrain peak conditions in the migmatitic paragneisses across de NVC to $820^{\circ}\text{C} \pm 30^{\circ}\text{C}$ at 6.5 ± 0.5 kbar (Munhá et al. 2005) and 750°C to 930°C at 6.1 ± 1.5 kbar (Gradim et al. 2014) with the use of inverse thermobarometry; and 750°C to 1000°C at 6 to 9 kbar (Richter et al. 2016) and 732°C to 883°C at 5.6 to 7.3 kbar (Wisnioski et al. 2020) based on more recent phase equilibrium modelling work. Retrograde conditions of 640°C - 800°C and 4.5–6 kbar were constrained by Richter et al. (2016), defining a clockwise P-T evolution for these rocks. Timing of near-peak conditions is constrained by U-Pb dating of zircon and monazite to have occurred at 560–571 Ma, whereas retrograde conditions ($<700^{\circ}\text{C}$) occurred at circa 500 Ma (Richter et al. 2016; Wisnioski et al. 2020). Metamorphic conditions from the outcrop studied in this work have previously been constrained at 970°C - 1010°C and 5.6–6.0 kbar for proximal hornfels next to a noritic gabbro (Wisnioski et al. 2020).

2.2 | Ediacaran and Cambrian-Ordovician Intrusive Rocks

Intrusive Ediacaran peraluminous and metaluminous rocks and Cambrian-Ordovician high-temperature magmatic units occur within the Nova Venecia complex (Figures 1c and 2a). These rocks occur as garnet-bearing peraluminous granitoids, with dominant granodioritic and granitic compositions and contain abundant enclaves of paragneisses and calcsilicate rocks, indicating their genetic relationship to the migmatites of the Nova Venecia complex (Gradim et al. 2014; Cavalcante et al. 2021). The granitoids occur at different scales, from leucocratic veins to large massifs of foliated granitoids (Figures 1c and 2a). Crystallization ages for these rocks range from ~590 to 570 Ma; however, younger U-Pb dates (ca. 570–550 Ma) for monazite and zircon grains highlight complex recrystallization

(metamorphic/metasomatic?) and/or isotopic reequilibration processes (Melo et al. 2017a, 2017b; Cavalcante et al. 2021).

Additional intrusive rocks including metaluminous I-type granitoids, ranging from hornblende-bearing granitoids to enderbites and charnockites, and gabbro-norites (Pedrosa-Soares and Wiedemann-Leonardos 2000; De Campos et al. 2016) are also present. These rocks do not exhibit deformation fabrics and are interpreted as recording lower to middle crust geodynamics during the late gravitational collapse of the Araçuaí orogen (e.g., De Campos et al. 2016; Temporim et al. 2023). Most ages for this late-orogenic magmatism are around 500 Ma, but ages as old as ~535 Ma and young as 490–480 Ma have been found (De Campos et al. 2016; Melo et al. 2020). In the studied area, a gabbroic stock associated with this late-stage magmatism is referred to as the São Gabriel pluton (Figure 2a,b). It comprises melanocratic to mesocratic isotropic medium- to coarse-grained gabbro-norite. U-Pb SHRIMP zircon data for this gabbroic rock constrain its crystallization age at 523 ± 7 Ma (Wisnioski et al. 2020).

3 | Methods

3.1 | Petrography and Mineral Chemistry

Mineral chemistry data were obtained using the Electron-Probe Microanalyzer (EPMA) JEOL-JXA8600 in the Microprobe Laboratory at the São Paulo State University (UNESP) and at the University of São Paulo (USP). For spot analysis, the equipment was operated with 15 keV of accelerating voltage, 20-nA current, 5- μm beam diameter (except for 3- μm biotite that was used and USP points with 10 μm) and 10-s peak dwell time (5 s in background) for elements with expected concentrations >5%; and 20 s peak dwell time (10 s in background) for elements with expected concentrations <5%. Compositional maps were obtained using the same operational conditions at UNESP (15 keV, 20 nA), but 200 ms of dwell time, following the procedures described in Lanari et al. (2019). Si, Al, Fe, Mg, Mn, Ca, Na, K, P and Ti were analysed using wavelength dispersive spectrometer (WDS) detectors, and Cr, S, Zn and Zr were determined with energy dispersive spectrometer (EDS) detectors. Quantitative compositional maps were extracted using the internal standard technique (De Andrade et al. 2006) in the software XMapTools (Lanari et al. 2014; Lanari and Engi 2017). Additional maps of structural formula and end-member compositions (e.g., Xalm, Xan, Al^{IV} and Si apfu) were also produced using XMapTools. The specific parameters for the X-Ray maps and representative spot data used for standardization are presented on Data S1.

3.2 | Thermodynamic Modelling

The isochemical phase diagrams were calculated using the software THERIAK-DOMINO (De Capitani and Petrakaki 2010) and the thermodynamic database tcds55_p07.bs (Holland and Powell 1998). The solid solution models used for calculations in the MnNCKFMASHTO chemical system were listed as follows: White et al. (2007) for silicate melt; White et al. (2005) for biotite, garnet and ilmenite; White et al. (2002) for orthopyroxene; Holland and Powell (1998) for cordierite and spinel; and Holland and Powell (2003) for plagioclase and K-feldspar. The

H₂O and ferric iron contents were estimated using T-X phase diagrams (Data S2). Chemical compositions were extracted from compositional maps using XMapTools (Lanari et al. 2019).

3.3 | Geochronology and REE Geochemistry

3.3.1 | U-Pb Zircon Dating and REE Analysis

Samples processed for zircon geochronology were crushed, milled and sieved. Magnetic separation was attained using the Frantz magnetic separator and/or a Nd hand magnet. Selected zircon grains representing different morphologies, colours and inclusion presence were hand-picked and mounted on epoxy resin mounts, polished and then carbon coated for cathodoluminescence (CL) and backscattering electron imaging, performed at the University of Campinas (UNICAMP) with a SEM model Zeiss Leo 430i and a Gatan Chroma CL DIGISCAN II CL detector. These images were used to select spot locations, considering possible fractures and chemical zoning. The system used for isotopic analysis was the LA-ICP-MS installed at the *Laboratório de Geologia Isotópica* (LAGIS-UNICAMP), with the mass spectrometer Thermo Fisher Scientific Element XR, attached to a Photon Machine Excites 193 module and the HelEx ablation cell. Laser conditions were 25- μm spot diameter, 10-Hz repetition rate and $\sim 4.75 \text{ J/cm}^2$ fluence with 40 s of dwell time for the analysis. The routine comprised two standard analyses, 1 blank and 10 unknowns. The standards used were Peixe (²⁰⁶Pb/²³⁸U age of 564 Ma; Gehrels, unpublished) and 91500 (²⁰⁶Pb/²³⁸U TIMS age of 1065.4 ± 0.6 Ma; Wiedenbeck et al. 1995). Both standard results are presented in Data S5 and are in accordance with reference data. Data were reduced and filtered with the IOLITE module of software Igor Pro (Paton et al. 2011), visualized with module VizualAge (Petrus and Kamber 2012) and plotted with IsoplotR (Vermeesch 2018). REE analyses were also obtained by the same ICP-MS laser ablation system, with the same spot size and fluence from the U-Pb analyses, and spot locations were chosen right next to the U-Pb spots, maintaining textural/domain control. Spot locations are presented with geochronological data figures. Ablation time for REE analyses was 90 s (30 s for gas blank and 60 s for sample counting).

3.3.2 | Lu-Hf and Sm-Nd Garnet Dating and REE Analysis

Sample preparation for garnet dating included the isolation of garnets from whole-rock samples after crushing, milling, sieving and magnetically separating the samples to a specific grain size, controlled by the diameter of the target garnet population. Four 250-mg garnet fractions plus 500 mg of garnet-free whole-rock fractions were isolated for Lu-Hf analysis. Three 100-mg garnet fractions and one whole-rock fraction were isolated for Sm-Nd analysis. For Sm-Nd analysis, two size fractions were used (two garnet fractions 125–63 μm , one <63 μm) to ensure greater surface area and exposure of possible high-Nd inclusions (e.g., monazite and apatite). The Lu-Hf and Sm-Nd garnet dating was performed in the Radiogenic Isotope and Geochronology laboratory (RIGL) at Washington State University following the procedures from Johnson et al. (2018) and Anczkiewicz and Thirlwall (2003). Pure Lu, Hf, Sm and Nd solutions were analysed using a Thermo Fisher Scientific Neptune Plus multicollector ICP-MS. The constant

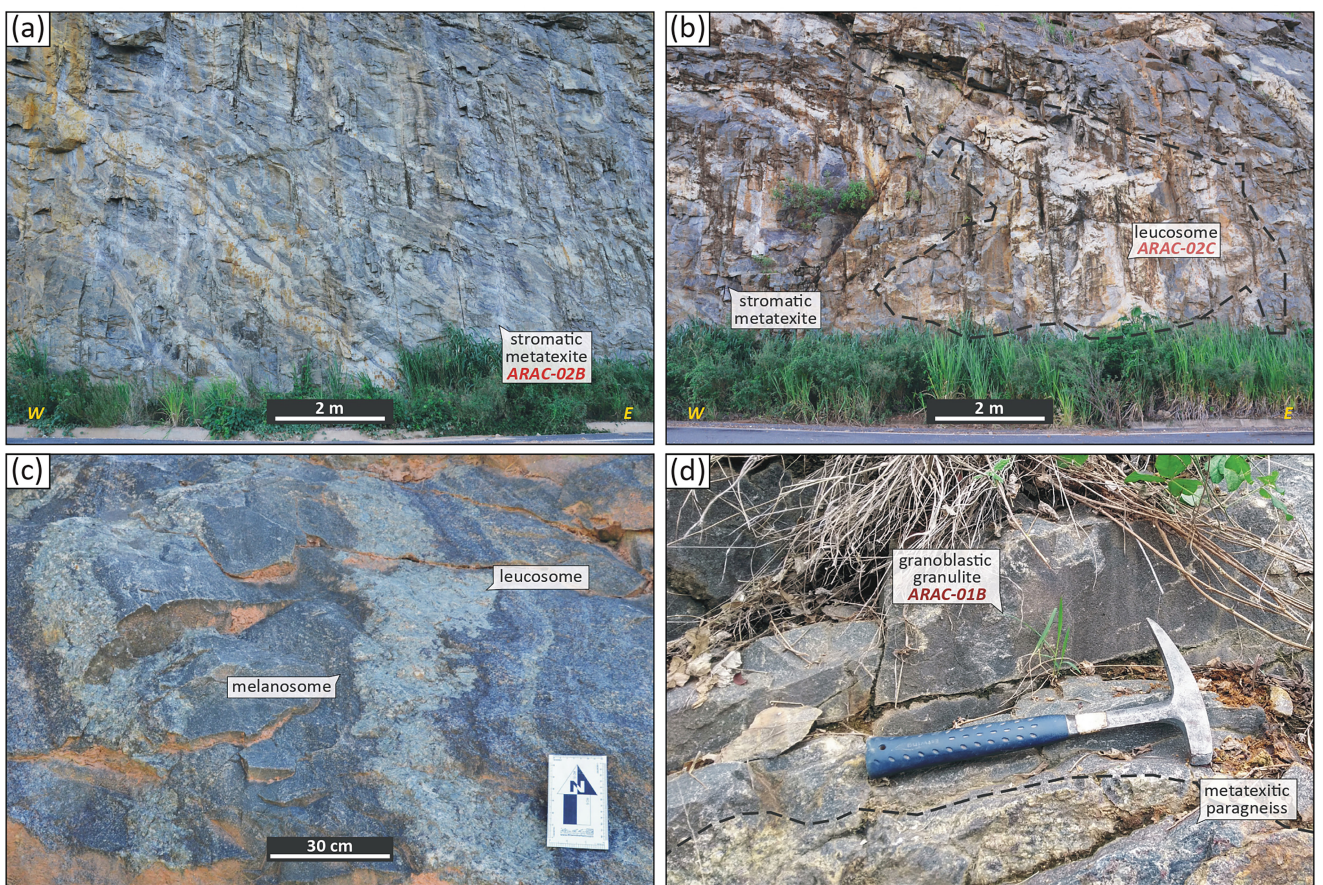


FIGURE 3 | Field features of the migmatitic paragneisses. See location of the photos in the outcrop sketch (Figure 2c). Sampling locations are also highlighted. (a) Stromatic metatexitic paragneiss (ARAC-02B); (b) in-source leucosome parallel to the gneissic banding (ARAC-02C); (c) leucosome and melanosome segregation pairs occurring in the western part of the outcrop; (d) contact between the cordierite-garnet granoblastic granulite (ARAC-01B) and the stromatic metatexitic paragneiss (westernmost part of the outcrop).

decays used for age calculations were $1.867 \times 10^{-12} \text{ a}^{-1}$ for ^{176}Lu (Söderlund et al. 2004) and $6.54 \times 10^{-12} \text{ a}^{-1}$ for ^{147}Sm (Lugmair and Marti 1978). Data reduction procedures followed Vervoort et al. (2004) and references therein.

Garnet REE analysis was done at Western Washington University using an Agilent 7500ce ICP-MS coupled with the New Wave Research UP-213AS LA Accessory. Ten (10) spots were chosen in one representative garnet grain avoiding central inclusions, in a profile from rim to rim. Parameters used were the following: spot size, $40 \mu\text{m}$; dwell time, 90s (120s of total acquisition time, including 30s of background); fluence, $\sim 13 \text{ J/cm}^2$; repetition rate, 10Hz; and laser energy output of 80%. Calibration was performed using values obtained by Jochum et al. (2011) from the NIST 610 and 612 SRM (Pearce et al. 1997), and data were reduced in the software Glitter v.4.4.4 (Van Achterbergh et al. 2000).

4 | Field Geology

The field descriptions presented in this manuscript are based on observations made at a large roadcut spanning approximately 250 m, near Colatina city in Espírito Santo State, Brazil (Figure 2a,b). Additional observations were gathered from active quarries in the vicinity (Figure 2a). This extensive roadcut reveals various field features of the migmatitic paragneisses from the Nova Venecia

complex and the contact of this sequence with the late-orogenic gabbro-norite of the São Gabriel pluton (Figure 2c). This key outcrop was also studied by Wisniowski et al. (2020).

The main lithotype in the outcrop is a metatexitic cordierite-garnet paragneiss (\pm orthopyroxene \pm spinel \pm sillimanite) with prominent stromatic structures (Figures 2c and 3a) and, locally, folded structures defined by in-source leucosome. Gneissic banding is marked by compositional layering/intercalations of quartz/feldspar-rich coarse-grained felsic bands and biotite-rich bands with garnet, orthopyroxene and cordierite. Leucosomes occur as garnet-bearing bands oriented parallel to the gneissic banding and as coarser sub-metric folded bands (Figure 3a,b). Leucosome and melanosome segregation pairs are locally observed (Figure 3c). These pairs have more diffusive contacts between layers and are generally concordant to foliation. Melanosomes are coarse- to medium-grained and rich in cordierite, garnet, orthopyroxene and biotite. Fine- to medium-grained granoblastic cordierite-garnet granulites are present in the westernmost part of the outcrop and are intercalated within the stromatic metatexitic paragneiss (Figures 2c and 3d).

The São Gabriel pluton is mapped as an irregular 'V'-shaped intrusion that is approximately 4–6 km in length (Figure 2a). It is a homogeneous isotropic medium- to coarse-grained gabbro-norite, extensively exploited as ornamental stone (commercially known as

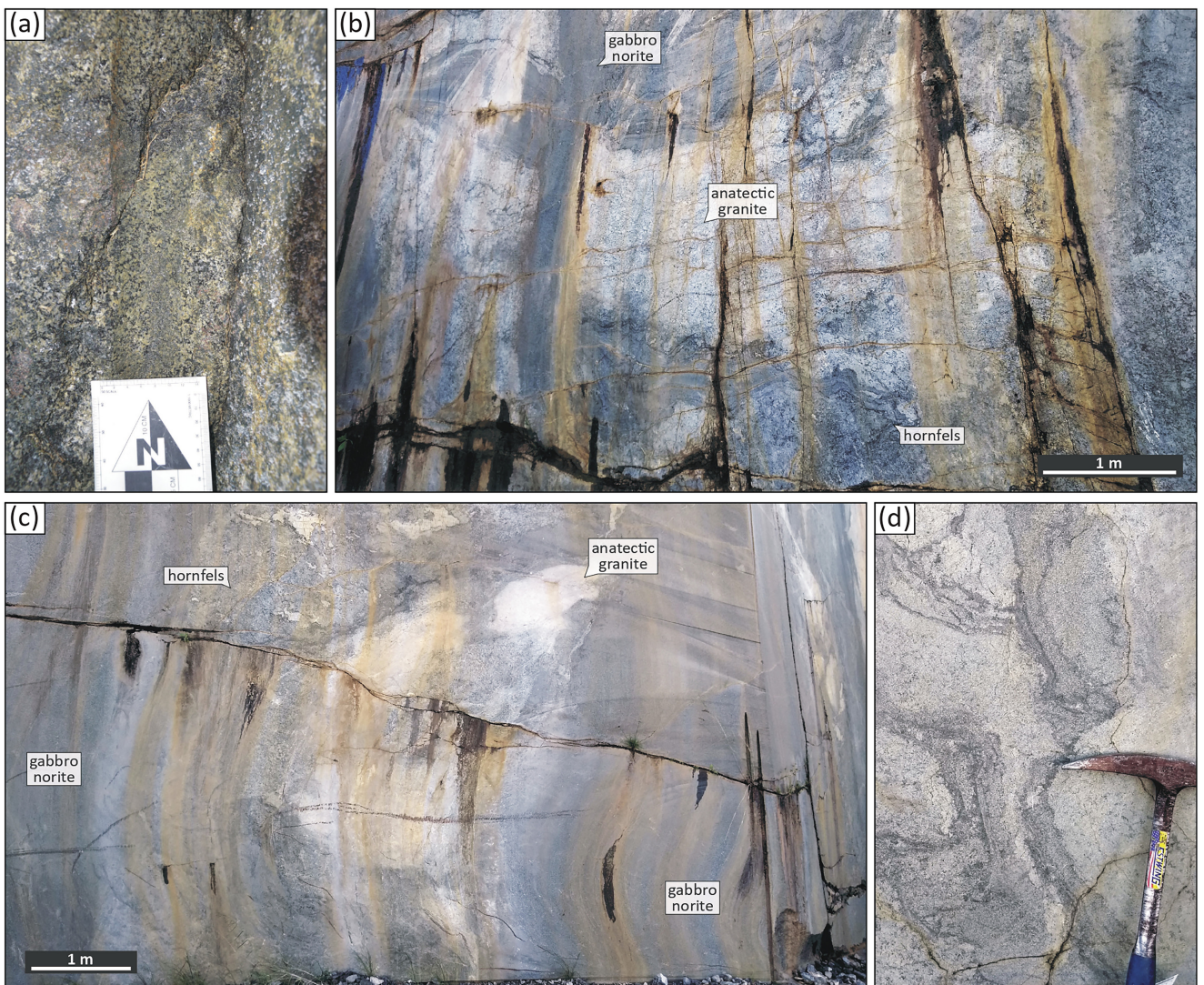


FIGURE 4 | Field features from the complex contact domain between migmatitic paragneisses and gabbro-norites (see location in Figure 2b, ARAC-12). (a) Equigranular granoblastic orthopyroxene-rich hornfels; (b,c) contact domain of the migmatitic paragneisses and the gabbro-norite showing the diffuse character of this interface and the complex pattern of molten rocks interaction; (d) magmatic flow structures defined by biotite-rich schlieren in anatetic melts within the diffuse contact between the migmatitic paragneisses and the gabbro-norite.

'San Gabriel Black Granite') and its mineralogy comprises orthopyroxene, clinopyroxene, plagioclase and minor hornblende, biotite and quartz. Despite being a homogeneous igneous body, its interface with the host migmatitic paragneiss exhibits complex patterns of interaction between molten rocks (Figure 4), distinctly different from the abrupt contact depicted in the sketch of Figure 2c. Next to the contact with the gabbro-norite, coarse-grained granoblastic hornfels are observed (Figure 4a). Within this interface domain, leucocratic garnet-bearing rocks, hornfels and gabbro-norite are mixed together in a complex pattern (Figure 4b,c). Magmatic flow structures, such as biotite-rich schlieren, are observed in the leucocratic rocks (Figure 4d).

5 | Sample Descriptions and Mineral Chemistry

Detailed petrographic studies were carried out on cordierite-garnet granulites, metatectic paragneiss, in-source leucosomes and hornfels. Additional petrographic features are present in

Data S3, whereas full mineral chemistry data and additional compositional maps are presented in Data S4. Mineral abbreviations adhere to the conventions from Whitney and Evans (2010).

5.1 | Al-Rich Granulitic Paragneiss

The baric peak assemblage of the granulitic paragneiss in the western and central parts of the studied outcrop is composed of garnet, orthopyroxene, plagioclase, K-feldspar, quartz, biotite, sillimanite and ilmenite, showing distinct textures according to different microdomains. Garnet occurs as medium- to coarse-grained subidioblastic to xenoblastic grains, commonly forming poikiloblastic textures wrapped by the regional gneissic fabric (Figure 5a). These garnet grains are usually associated with aggregates of biotite, ilmenite and quartz (Figure 5a,b), but orthopyroxene is locally observed (Figure 5b,c). Acicular sillimanite (fibrolite) is also present. In these microdomains, orthopyroxene occurs as xenoblastic grains being replaced by biotite and quartz (Figure 5c), and

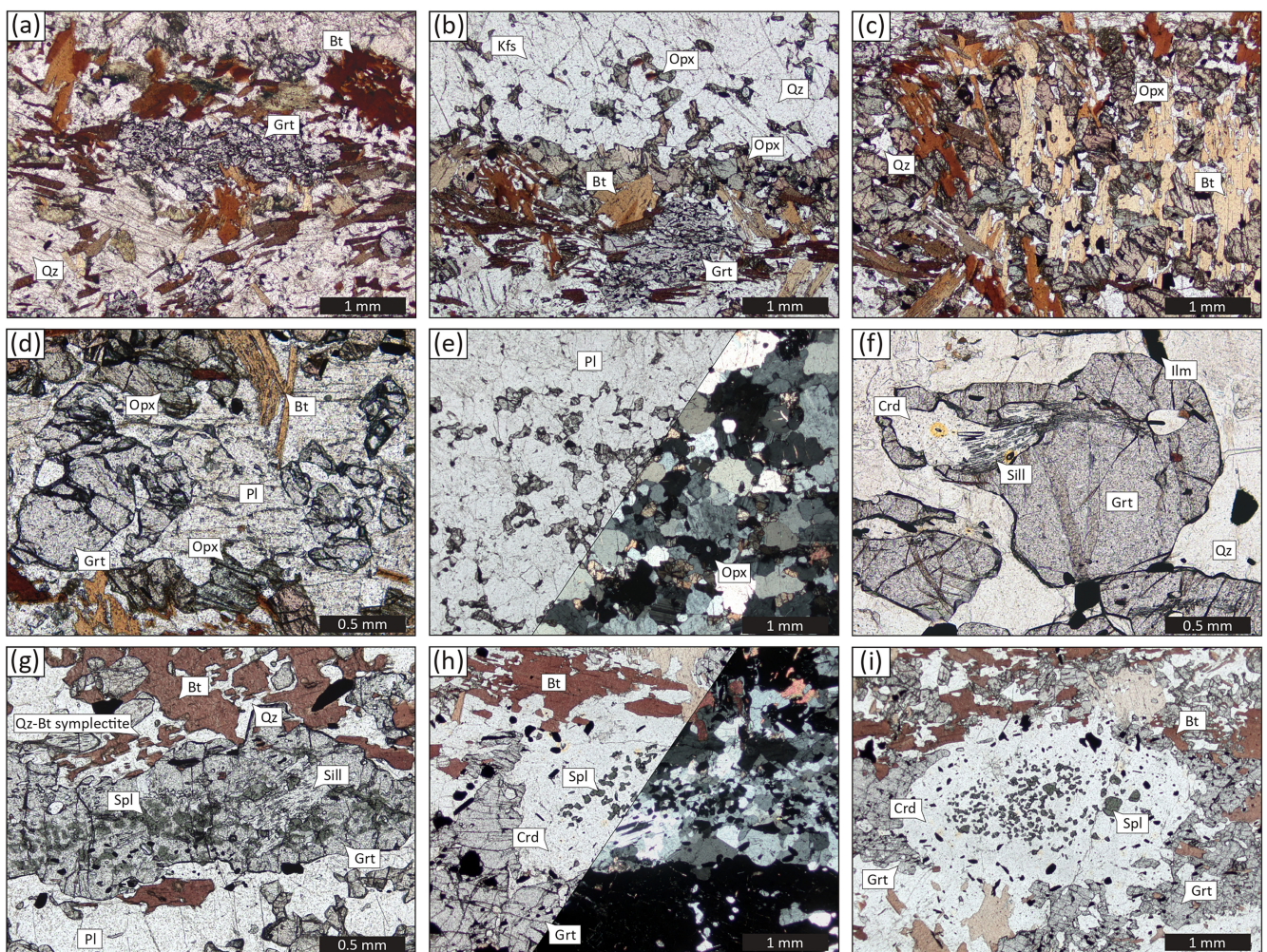


FIGURE 5 | Textural features observed in Al-rich granulitic paragneisses sampled in the west and central part of the studied outcrop. (a) Xenoblastic and poikiloblastic garnet oriented parallel to rock foliation with corroded rims of subhedral biotite and plagioclase; (b) xenoblastic garnet with biotite and plagioclase rims associated with subidioblastic/xenoblastic fine-grained orthopyroxene in the limit between the garnet-rich microdomain and a fine-grained interstitial orthopyroxene microdomain; (c) mafic orthopyroxene-rich layers with medium- to coarse-grained subidioblastic orthopyroxene, idiomorph biotite and local biotite and quartz; (d) xenoblastic garnet rimmed by irregular-shaped films/veinlets of plagioclase; (e) felsic plagioclase-rich equigranular domain with interstitial fine- to medium-grained orthopyroxene and minor biotite and ilmenite grains; (f) medium-grained subidioblastic clean garnet with oriented fine-grained sillimanite associated with cordierite clustering with zircon inclusions marked by a pleochroic halo; (g) xenoblastic poikiloblastic garnet with spinel and sillimanite inclusions. Garnet is rimmed by irregular shaped intergrowths of plagioclase and biotite; (h,i) replacement textures with the assemblage cordierite-spinel-ilmenite-zircon replacing garnet + sillimanite (*Texture 1*).

as subidioblastic grains associated with garnet but being replaced by plagioclase (Figure 5d). In felsic microdomains, orthopyroxene occurs as interstitial xenoblastic grains within medium-grained matrix plagioclase (Figure 5e). Replacement textures are well defined in locally embayed garnet porphyroblasts around cordierite, which is associated with sillimanite (Figure 5f), spinel and zircon (Figure 5g-i). These textures highlight the consumption of garnet and formation of cordierite (Figure 5f), often associated with biotite/quartz symplectites (Figure 5g) and the development of spinel aggregates (Figure 5h,i).

5.1.1 | Cordierite-Garnet Granulite With Spinel + Sillimanite (ARAC-01B)

Sample ARAC-01B represents a cordierite-garnet granulite that occurs as greyish medium-grained equigranular boudins/lenses

hosted by the metatexitic paragneiss, subparallel to the gneissic banding (Figure 3d) in the westernmost part of the outcrop (Figure 2c). The rock shows a general granoblastic texture marked by subidioblastic, usually fractured, garnet crystals with an average diameter of 0.1 mm and not larger than 2.5 mm, plus quartz and feldspars (perthitic alkali feldspar + plagioclase). Biotite occurs locally as interstitial grains (Figure 6a). Garnet inclusions comprise very fine- to fine-grained sillimanite (fibrolite) trails (Figure 6a) and surrounded fine-grained quartz grains, concentrated mainly in cores. Quartz and feldspars form a felsic coarse- to medium-grained matrix, dominated by medium- to coarse-grained perthitic alkali feldspar (average diameter of 1 mm) and fine- to medium-grained quartz and plagioclase. Textures characterized by garnet around aggregates of cordierite, hercynitic spinel, ± sillimanite and ± ilmenite are common. Zircon and monazite are also common (Figure 6b,d, see Data S3), as well as aggregates of cordierite, sillimanite, hercynitic spinel, ilmenite and alkali feldspar

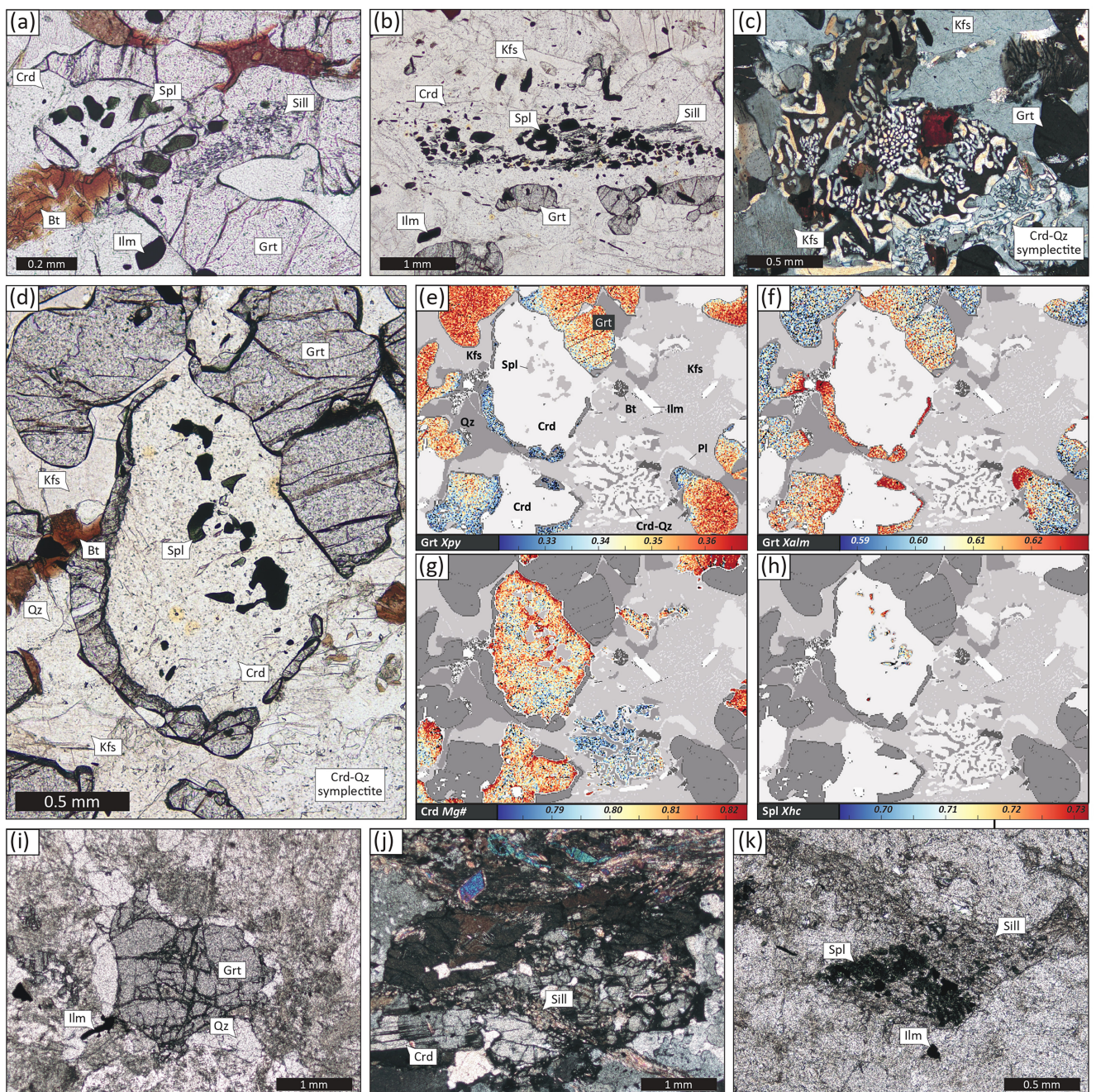


FIGURE 6 | (a–h) Textural features of the modelled cordierite-K-feldspar-garnet granulite with spinel + sillimanite (sample ARAC-01B) and (i–k) in-source leucosome (ARAC-02C). (a) Very fine-grained fibrolite trail within xenoblastic garnet and small and rounded spinel rimmed by very thin films of cordierite within garnet and coarser cordierite and spinel clusters; (b) stretched cordierite-spinel-sillimanite-ilmenite cluster (*Texture 1*) within K-feldspar-rich felsic matrix; (c) cordierite-quartz symplectite within K-feldspar-rich matrix; (d) texture including garnet-cordierite-spinel mineral assemblage (*Texture 1*) selected for modelling; (e–h) examples of compositional maps: (e) garnet X_{Py} and (f) X_{Alm}; (g) cordierite Mg#; (h) spinel X_{Hc}; (i) xenoblastic garnet with leucocratic irregular films on its border; (j) medium-coarse cordierite knot with associated fibrolite within quartz-feldspathic matrix; (k) possible garnet pseudomorph sillimanite + spinel cluster.

(Figure 6b). Cordierite/quartz symplectites also occur (Figure 6c). These garnet textures and aggregates of cordierite+spinel are referred to as *Texture 1* (Figure 6d). Zircon and monazite grains occur as accessory minerals within the garnet texture (Data S3). Monazite inclusions in garnet are also present.

Chemical composition in garnet varies from X_{Alm}=0.59–0.66, X_{Prp}=0.29–0.37, X_{Grs}=0.02–0.03 and X_{Sps}=~0.02. The

chemical variation is subtle in the subidioblastic garnet grains and cores from xenoblastic garnet associated with *Texture 1* clusters (X_{Prp}=0.33–0.37, X_{Alm}=0.59–0.63). However, rims in the vicinity of *Texture 1* close to cordierite have slightly lower pyrope and higher almandine contents (X_{Prp}=0.32–0.36, X_{Alm}=0.60–0.64) (Figure 6e,f). Cordierite is chemically homogeneous (Mg#=0.75–0.84), but slightly higher Mg# is seen in the contacts with garnet and spinel (Mg#=~0.82) and the lowest Mg#

occurs in the cordierite/quartz symplectites ($Mg\# = \sim 0.78-0.79$) (Figure 6g). Spinel is also chemically homogeneous and is classified as hercynitic spinel (hercynite component ranges from 0.64 to 0.77, and spinel contents varies from 0.23 to 0.36) (Figure 6h) with low ZnO contents (2.25–2.64 wt%). Perthitic alkali feldspar exhibits an orthoclase component ranging from 0.68 to 0.92 (non-integrated composition), with a slight increase in orthoclase contents observed from core to rim, particularly noticeable on thin rims poor in albitic lamellae (Data S4). Plagioclase is homogeneous and classified as an oligoclase (albite component varying from 0.71 to 0.80). Biotite has iron contents ($FeOt$) varying between 11.30 and 15.61 wt%, aluminium contents (Al total) ranging from 2.74 to 2.90 apfu, $Mg\#$ between 0.57 and 0.72 and high Ti contents between 0.38 and 0.66 apfu.

5.1.2 | Orthopyroxene-Cordierite-Garnet Porphyroblastic Granulite With Spinel + Sillimanite (ARAC-02B)

Sample ARAC-02B corresponds to a medium- to coarse-grained porphyroblastic metatexitic paragneiss with orthopyroxene, garnet, cordierite, spinel, and sillimanite. Idioblastic to subidioblastic garnet porphyroblasts (up to 2 cm in diameter) show inclusions of rounded quartz, biotite, and ilmenite, and are usually fractured (subparallel planar fractures) (Figure 7a). Replacement textures are present in this sample, showing smaller garnet grains around cordierite and spinel aggregates associated with zircon and monazite

(Figure 7a). These aggregates are usually oriented parallel/subparallel to the regional foliation (i.e., gneissic banding). This texture is referred to as *Texture 2* and was used in thermodynamic modelling below. Larger microdomains rich in cordierite, spinel and sillimanite also occur in this sample (Figure 7b). Subidioblastic to xenoblastic orthopyroxene occurs in mafic bands associated with garnet and biotite, and in felsic bands associated with plagioclase and quartz (Figure 7c). Orthopyroxene shows brownish Ti exsolution lamellae. The felsic bands are predominately plagioclase and quartz, but alkali feldspar is locally observed. Idioblastic oriented biotite occurs parallel to the foliation (Figure 7a). Biotite grains develop rims around orthopyroxene and garnet (Figure 7c) and may form symplectites with quartz.

Garnet porphyroblasts show larger variation in chemical composition ($X_{alm} = 0.59-0.64$, $X_{prp} = 0.29-0.36$, $X_{sp} = 0.01-0.04$ and $X_{gr} = 0.02-0.03$) with higher pyrope/lower almandine contents in the core. Medium-grained idioblastic to subidioblastic garnet crystals display more homogeneous chemical composition with higher almandine and pyrope contents ($X_{alm} = 0.57-0.59$ and $X_{prp} = 0.37-0.38$) and lower spessartine and grossular components ($X_{sp} = 0.02$, $X_{gr} = 0.03$). Xenoblastic and poikiloblastic garnet grains have lower pyrope contents ($X_{prp} = 0.29-0.36$), akin to the smaller garnet grains around the cordierite + spinel aggregates (*Texture 1*). These smaller garnet grains display higher almandine and lower pyrope contents than the idioblastic to subidioblastic grains ($X_{alm} = 0.61-0.64$ and $X_{prp} = 0.32-0.36$)

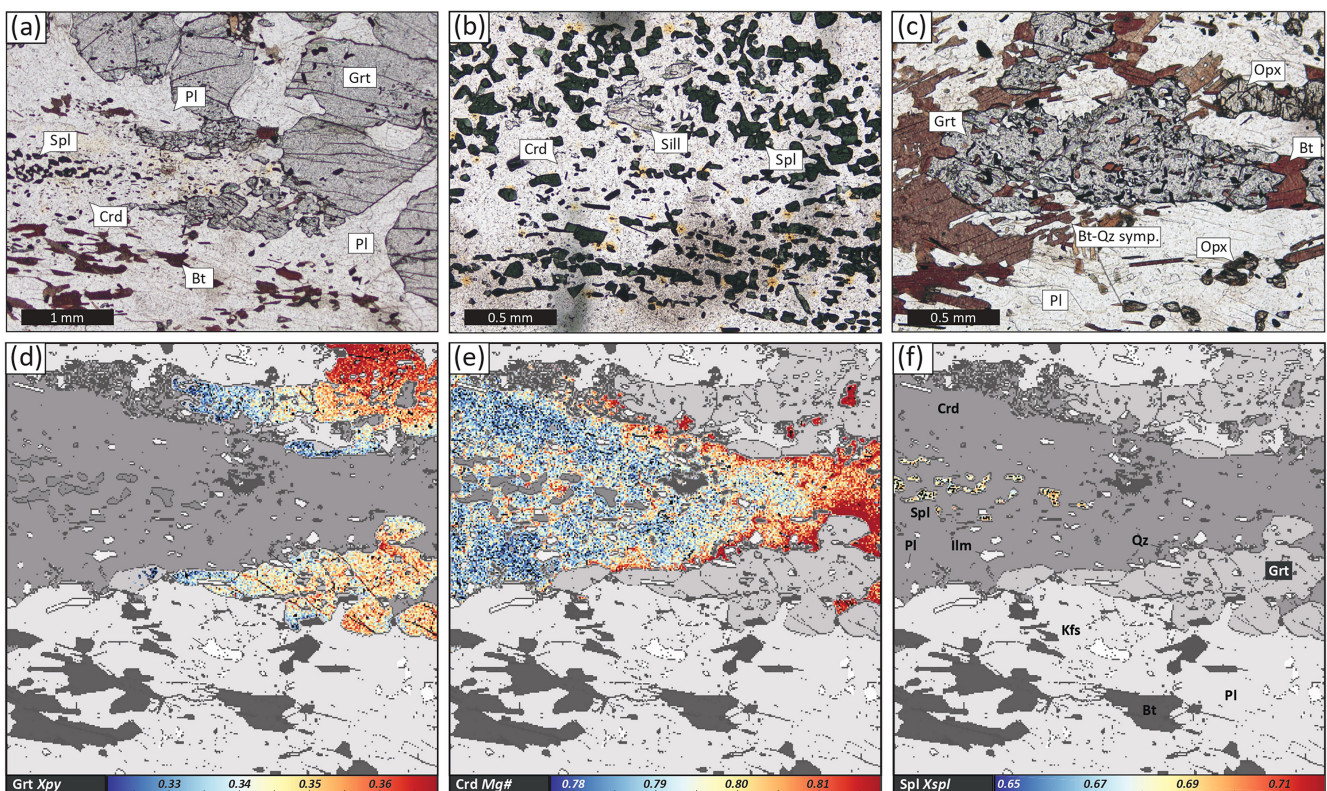


FIGURE 7 | Photomicrographs of orthopyroxene-cordierite-garnet porphyroblastic granulite with spinel + sillimanite (sample ARAC-02B). (a) General context of the modelled texture (*Texture 2*), including subidioblastic garnet being replaced by cordierite and spinel; (b) stretched cordierite-spinel-sillimanite microdomain parallel to the main foliation; (c) xenoblastic garnet grains with very fine-grained rounded inclusions of quartz, biotite and ilmenite, and subidioblastic orthopyroxene and plagioclase; (d-f) examples of compositional maps from *Texture 2*: (d) garnet X_{prp}; (e) cordierite Mg#; (f) spinel X_{sp}.

(Figure 7d). Orthopyroxene presents minor variations in Mg and Fe contents ($X_{\text{Mg}} = 0.53\text{--}0.56$; $X_{\text{Fe}} = 0.34\text{--}0.38$), and octahedral Al contents range from 0.03 to 0.08 apfu. Plagioclase is compositionally homogeneous and is classified as a sodic andesine ($X_{\text{An}} = 0.30\text{--}0.34$; $X_{\text{Ab}} = 0.62\text{--}0.67$), whereas alkali feldspar shows a considerable variation in orthoclase component ($X_{\text{Or}} = 0.79\text{--}0.97$). Cordierite displays small compositional variations ($\text{Mg}\# = 0.78\text{--}0.82$), with higher Mg contents close to the contact with garnet (Figure 7e). Spinel is a homogeneous hercynitic spinel with slight variations in hercynite (0.68–0.71) and spinel (0.29–0.32) (Figure 7f). Biotite shows high Ti contents between 0.33 and 0.70 apfu, iron contents (FeO/t) varying from 9.83 to 15.52 wt% and magnesium number ($\text{Mg}\#$) ranging from 0.57 to 0.75. The biotite grains associated with xenoblastic garnets and/or orthopyroxene show higher Ti contents (0.61–0.69) when compared with biotite within the quartz-feldspathic matrix (0.30–0.70, Data S5).

5.1.3 | In-Source Leucosome With Garnet + Cordierite + Sillimanite + Spinel (Sample ARAC-02C)

Sample ARAC-02C is a coarse-grained leucosome sampled exclusively for U-Pb zircon dating. The rock was sampled from a leucocratic pocket (see Figure 3b), where leucosome is segregated from the gneissic layering. The matrix shows intense cuspatate contacts between quartz and feldspars. Local subidioblastic

garnet grains are observed, showing rims of leucocratic quartz-feldspathic films (Figure 6i). Coarse cordierite-rich micro-domains associated with fibrolite are also present (Figure 6j), as well as aggregates of sillimanite and spinel resembling garnet pseudomorphs (Figure 6k). Melt films defined by quartz and/or feldspar are also present. Photomicrographs from sample 02C are presented on Data S3.

5.2 | Hornfels and Related Rocks

Rocks from the contact aureole between the São Gabriel pluton and the Al-rich granulitic rocks are referred to as hornfels and display similar mineral assemblages and textures to the other granulitic paragneisses in the outcrop. Textures such as granoblastic interlobate orthopyroxene with plagioclase (Figure 8a), subidioblastic garnet grains in a plagioclase-rich matrix (Figure 8b), in leucosome microdomains with spinel inclusions (Figure 8c) and aggregates of spinel-sillimanite-plagioclase ± cordierite ± garnet (Figure 8d,e) are similar to the microstructures described in Figures 5–7. Orthopyroxene-rich bands associated with coarse-grained biotite grains (Figure 8e) and garnet are also common. The predominant feature exclusively described within the contact aureole is distinctive atoll textures. These textures are defined by orthopyroxene surrounding spinel, separated by a thin layer of plagioclase (Figure 8f) and occur specifically within the granoblastic orthopyroxene + plagioclase microdomain.

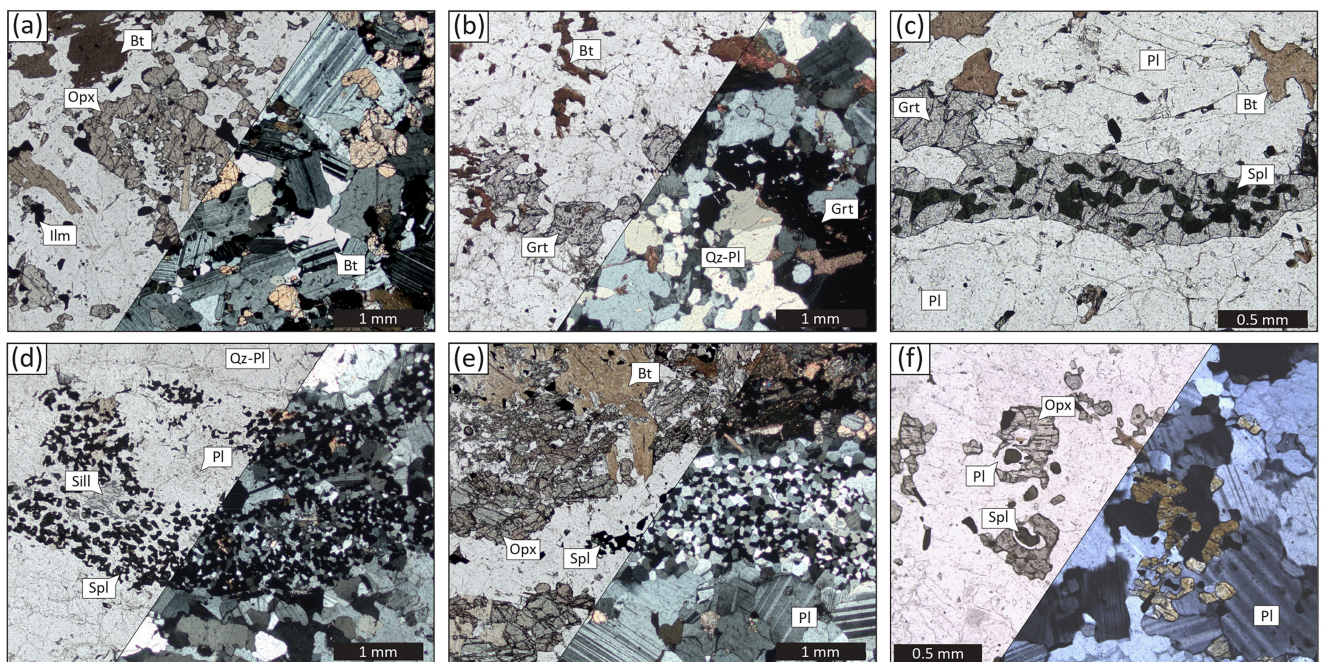


FIGURE 8 | Textural features observed in the rocks near the São Gabriel pluton, at the easternmost part of the studied outcrop. (a) Xenoblastic to subidioblastic interstitial orthopyroxene within felsic inequigranular plagioclase-rich microdomain; (b) medium-grained subidioblastic to xenoblastic garnet grains within a felsic inequigranular plagioclase-rich matrix, including interstitial biotite and minor ilmenite; (c) xenoblastic garnet with spinel inclusions; (d) sillimanite-ilmenite-spinel cluster, with dominance of equigranular fine-grained spinel, within a coarse-grained plagioclase-rich matrix and local retrograde biotite; (e) plagioclase-spinel-ilmenite cluster oriented sub-parallel to main foliation. Fine-grained equigranular spinel occurs mainly in the inner part of the cluster. Plagioclase in the outer rim of the cluster is coarser than plagioclase within the cluster's core; (f) general context of the atoll-like texture (Texture 4): plagioclase-rich matrix with interstitial orthopyroxene, local orthopyroxene around plagioclase and spinel form the atoll-like textures. All photomicrographs (a, b, d, e and f) show diagonal split plane and cross polarized light, except (c) showing plane polarized light picture.

5.2.1 | Spinel-Orthopyroxene-Cordierite-Garnet Hornfels (ARAC-03R1)

The hornfels sample ARAC-03R1 displays two primary textures: a granoblastic texture with garnet, plagioclase and orthopyroxene, labelled as *Texture 3*; and the atoll textures unique to the hornfels domain, denoted as *Texture 4*. *Texture 3* is characterized by coarse-grained xenoblastic garnet (up to 1–1.5 mm of diameter) and subidioblastic orthopyroxene (average length of 0.7 mm) within an inequigranular fine- to medium-grained matrix rich in quartz and plagioclase, and minor K-feldspar (Figure 9a,b). Cordierite is also present in this association with interlobate contacts with K-feldspar and plagioclase (Figure 9b). Garnet shows fine-grained rounded inclusions of quartz, ilmenite and biotite (Figure 9b,c), and orthopyroxene contains brownish Ti exsolution lamellae (Figure 9a–c). In *Texture 3*, garnet has

almandine contents varying between 0.55 and 0.61 and pyrope component ranging from 0.34 to 0.40 (Figure 9d). Grossular and spessartine components vary slightly between 0.03–0.04 and 0.01, respectively. Orthopyroxene displays homogeneous composition with enstatite component around 0.51–0.59 and octahedral Al at around 0.05–0.14 apfu (Figure 9e). Cordierite is also compositionally homogeneous with Mg# around 0.76–0.81, but slightly higher Mg# values (~0.81) are found close to the contact with plagioclase, orthopyroxene, and garnet (Figure 9f). Anorthite contents in plagioclase vary from 0.33 to 0.42, with enrichment of Xan towards the cores (Data S6). K-feldspar shows more variable compositions with orthoclase and albite contents varying between 0.75–0.96 and 0.04–0.20, respectively. The higher orthoclase values are usually displayed towards the rims. Biotite grains are rare and display slightly variable composition, Mg#=~0.68–0.79 and Ti contents between 0.51 and 0.80 apfu.

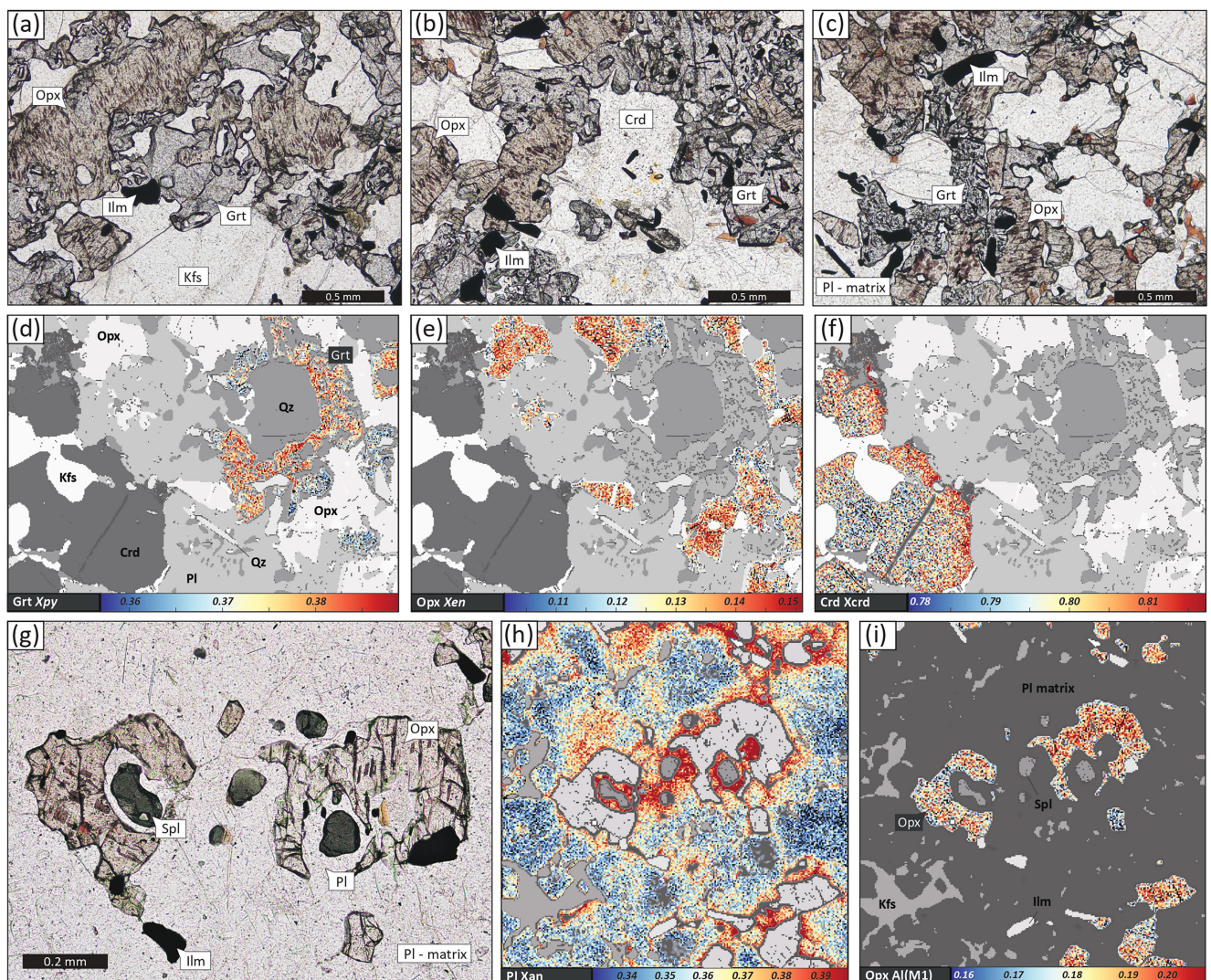


FIGURE 9 | Textures from the spinel-orthopyroxene-cordierite-garnet hornfels (ARAC-03R1). (a,b) General orthopyroxene-garnet association in contact with K-feldspar, cordierite and quartz. Garnet is xenoblastic and can display very fine-grained inclusions/symplectites of quartz and ilmenite; (c) general context of the modelled texture for the granulitic texture (*Texture 3*); (d–f) examples of compositional maps: (d) garnet Xprp; (e) orthopyroxene Xen; (f) cordierite Mg#. The local-bulk composition used for thermodynamic modelling were extracted from this map; (g) atoll-like texture (*Texture 4*) showing orthopyroxene around spinel separated by thin film of plagioclase—note the brownish Ti-exsolution lamellae in orthopyroxene; (h,i) examples of compositional maps: (h) plagioclase Xan; (i) orthopyroxene Al (M1-site). Compositional maps used to extract local-bulk compositions for thermodynamic modelling.

Texture 4 is characterized by orthopyroxene surrounding spinel, separated by thin layers of plagioclase (Figures 8f and 9g). Local fine-grained biotite grains are observed in the border of orthopyroxene. The matrix plagioclase is subhedral, fine- to medium-grained (~0.5–1.0 mm) and optically continuous with the plagioclase within the thin layers that form the atoll textures. Chemically, the matrix plagioclase has anorthite content around 0.34–0.43, with higher anorthite values around orthopyroxene and within the atoll textures (Figure 9h). Orthopyroxene displays a lower enstatite component ($X_{\text{en}} = 0.46\text{--}0.50$) when compared with the orthopyroxene in the granoblastic texture, and considerably higher octahedral Al content, reaching up to 0.20 apfu, with an incipient enrichment towards the core (Figure 9i and Data S6). Spinel is compositionally homogeneous with a hercynitic component of 0.65–0.69 and Zn contents of 2.10–2.27 wt%. The fine-grained biotite displays a lower magnesium number than in *Texture 3* ($\text{Mg}^{\#} = 0.64\text{--}0.66$) and Ti contents ranging from 0.66 to 0.76 apfu.

TABLE 1 | Chemical compositions used for thermodynamic modelling extracted from compositional maps. H_2O and Fe^{3+} obtained through T-X phase diagrams (Data S2).

Sample (ARAC)	01B	02B	03R1	03R1
Oxide (wt%)	Full map	Full map	Full map— <i>Texture 3</i>	Full map— <i>Texture 4</i>
SiO_2	51.17	48.74	54.99	55.71
TiO_2	0.7	1.31	1.76	0.73
Al_2O_3	22.99	26.67	18.13	23.26
FeOt	13.07	10.07	11.04	4.65
MnO	0.3	0.01	0.12	0.04
MgO	6.22	6.02	8	2.91
CaO	1.19	2.81	2.08	5.8
Na_2O	1.04	2.76	1.69	5.37
K_2O	3.23	0.8	0.83	1.01
Total	99.89	99.17	98.65	99.49
DOMINO input (mol)				
Si	0.852	0.811	0.915	0.927
Ti	0.009	0.017	0.023	0.009
Al	0.451	0.523	0.356	0.456
F3	0.02	0	0	0
Fe	0.162	0.14	0.154	0.065
Mn	0.004	0	0.002	0
Mg	0.154	0.149	0.198	0.072
Ca	0.021	0.05	0.037	0.104
Na	0.033	0.089	0.055	0.173
K	0.069	0.017	0.018	0.021
H	0.135	0.104	0.096	0.05
Total	1.91	1.9	1.854	1.877

6 | Thermodynamic Modelling

Thermodynamic modelling was conducted on representative samples encompassing the cordierite-garnet granulite (01B), orthopyroxene-cordierite-garnet porphyroblastic granulite (02B) and spinel-orthopyroxene-cordierite-garnet hornfels (03R1). Table 1 presents the chemical composition used for forward thermodynamic modelling (isochemical phase diagrams).

6.1 | Cordierite-Garnet Granulite With Spinel + Sillimanite (ARAC-01B)

An isochemical phase diagram was calculated for the cordierite-garnet granulite, sampled in the westernmost part of the outcrop (Figure 2c) to constrain the near-peak pressure P-T conditions. Textural constraints, including sillimanite as inclusions within subidioblastic garnet grains, suggest the

near-peak pressure mineral assemblage of plagioclase, K-feldspar, garnet, biotite, ilmenite, quartz, sillimanite and liquid (melt) (Figure 6a,d,e), limiting the P-T estimate for this sample between 6.5 kbar (cordierite formation) and 10 kbar (sillimanite formation) and ~770°C (K-feldspar formation) and ~850°C (biotite and plagioclase loss) (Figure 10a,b). The calculated garnet volume (~29%) using the compositional map is comparable with the modelled garnet modal volume (Figure 10a), even though it is suggested by the texture that part of the garnet has been consumed after the formation of cordierite. The relationship between garnet consumption and cordierite growth is shown in the phase diagram by the decrease of garnet volume isomodes after the introduction of cordierite at lower pressures (Figure 10a). The measured contents of pyrope in garnet and anorthite in plagioclase ($X_{\text{pp}} = 0.36 \pm 0.02$; $X_{\text{An}} = 0.28 \pm 0.02$) suggest near-peak pressure conditions around 800°C and 9.5 kbar (Figure 10b).

6.2 | Orthopyroxene-Cordierite-Garnet Porphyroblastic Granulite With Spinel + Sillimanite (ARAC-02B)

The isochemical phase diagram modelled from the orthopyroxene-cordierite-garnet porphyroblastic granulite is presented in Figure 10c,d. The observed mineral assemblage of plagioclase, garnet, biotite, ilmenite, spinel, cordierite and liquid is constrained by the stability field at pressures from ~4.5 to 5.5 kbar and temperatures between 770°C and 870°C (Figure 10c). Observed mineral isomodes of garnet (~16%) and cordierite (~34%) are comparable with the modelled isomodes within the constrained stability field (Figure 10c). The appearance of cordierite constrains an upper barometric limit at around ~6 kbar (Figure 10c) for this sample, with modelled cordierite and garnet volumes indicating an earlier decompression path, reaching the modelled P-T conditions (~800°C–850°C and 5 kbar) from higher pressures (Figure 10c). Modelled mineral isopleths, including garnet rim pyrope contents ($X_{\text{pp}} = 0.33 \pm 0.02$), cordierite Mg# ($\text{Mg\#} = 0.78 \pm 0.02$) and spinel hercynite ($X_{\text{hc}} = 0.67 \pm 0.02$) suggest temperatures higher than 800°C (Figure 10d).

6.3 | Spinel-Orthopyroxene-Cordierite-Garnet Hornfels (ARAC-03R1)

For the hornfels sample, two isochemical phase diagrams were calculated to constrain the P-T conditions for compositions representing the *Textures 3* and *4*. The estimate based on the model obtained from the granoblastic texture composition (*Texture 3* full map composition) considered the observed mineral assemblage cordierite, garnet, orthopyroxene, plagioclase, ilmenite, quartz and liquid. K-feldspar observed in the texture (Figure 9c,d) is interpreted to represent melt crystallization, along with plagioclase and quartz. In this isochemical phase diagram, the garnet volume decreases towards lower pressures, specifically at conditions of cordierite stability (Figure 11a). Biotite stability constrains a minimum temperature at ~800°C–810°C for the considered mineral assemblage. The stability field of this mineral assemblage is constrained by pressures between 4.5 and 6 kbar, due to the

loss of garnet and formation of rutile at lower and higher pressures, respectively, and temperatures above 800°C, after the loss of biotite (Figure 11a). The decrease in garnet volume and increase in orthopyroxene volume in the modelled phase diagram (Figure 11a) are consistent with described replacement textures involving consumption of garnet and growth of orthopyroxene (Texture 3—Figure 9a–c), supporting the occurrence of a decompression stage following the pressure peak conditions. Furthermore, the observed mineral isopleths, including pyrope contents in garnet ($X_{\text{pp}} = 0.37 \pm 0.02$), octahedral Al in orthopyroxene ($\text{Al}^{\text{VI}} = 0.14 \pm 0.02 \text{ apfu}$) and anorthite in plagioclase ($X_{\text{An}} = 0.42 \pm 0.02$) suggest P-T conditions for the *Texture 3* at around 5.2–6 kbar and 820°C–870°C (Figure 11b).

In the phase diagram for the *Texture 4* full map composition, the orthopyroxene, spinel, plagioclase, ilmenite and liquid assemblage constrains the P-T conditions at 3.5–6 kbar and 890°C–1080°C (Figure 11c). K-feldspar observed in the compositional map (Figure 9i) and part of the plagioclase in the matrix are interpreted as representing melt crystallization. The lower and higher limits in pressure conditions for the constrained stability field are defined by the introduction of spinel and garnet loss, respectively (Figure 11c). The stability of spinel also constrains a minimum temperature of 850°C for the modelled sample (Figure 11c). The modelled changes in volume isomodes within the interpreted stability field, including decrease of orthopyroxene and increase of spinel, are compatible with a heating path for the formation of the observed texture (*Texture 4*—Figure 9g–i). Mineral isopleths including anorthitic component in plagioclase from the thin layers within the atoll ($X_{\text{An}} = 0.39 \pm 0.02$) and octahedral Al in atoll orthopyroxene ($\text{Al}^{\text{VI}} = 0.19 \pm 0.02 \text{ apfu}$) suggest P-T conditions for the atoll formation at approximately 4.5 kbar and 950°C (4–6 kbar and 900°C–1050°C; Figure 11d). The modelled isopleths for the observed spinel ($X_{\text{hc}} = \sim 0.65$) plot at lower temperatures than those in the modelled stability field, particularly in a field where biotite and cordierite are stable (Figure 11d). This inconsistency might arise from either chemical diffusion processes taking place during cooling or the failure to reach equilibrium during heating. Patchy chemical zoning observed in plagioclase and, to a lesser extent, in orthopyroxene (Figure 9h,i) further suggests the occurrence of chemical diffusion processes, which could be attributed to either cooling or heating events.

7 | Geochronology and REE Geochemistry

Zircon U-Pb and REE data from a cordierite-garnet granulite (ARAC-01B) and an in-source leucosome (ARAC-02C) are presented below, as well as Lu-Hf and Sm-Nd garnet data from sample ARAC-01B. All the data, including U-Pb, REE, Lu-Hf and Sm-Nd data, are fully presented in Data S7.

7.1 | Cordierite-Garnet Granulite With Spinel + Sillimanite (ARAC-01B)

Both garnet and zircon from the cordierite-garnet granulite sample were analysed for geochronology and REE. Zircon crystals

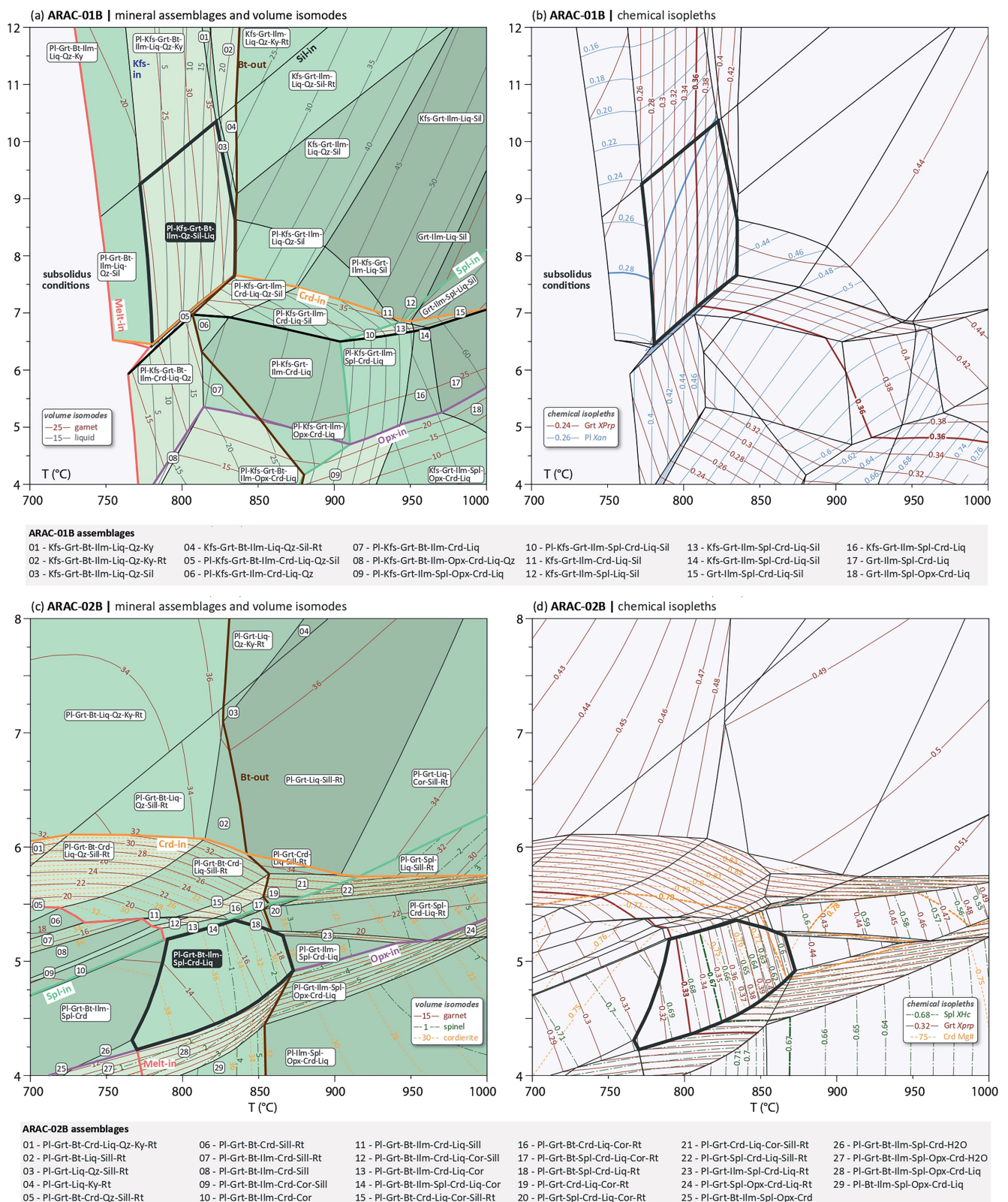


FIGURE 10 | Isochemical phase diagrams for samples ARAC-01B (a,b) and ARAC-02B (c,d) bulk compositions—see Table 1. (a) Sample ARAC-01B mineral assemblages and volume isomodes with main phase reactions; (b) sample ARAC-01B chemical isopleths; (c) sample ARAC-02B mineral assemblages and volume isomodes with main phase reactions; (d) sample ARAC-02B chemical isopleths. In parts (a) and (c), darker and lighter shades of green represent high and low variance fields, respectively.

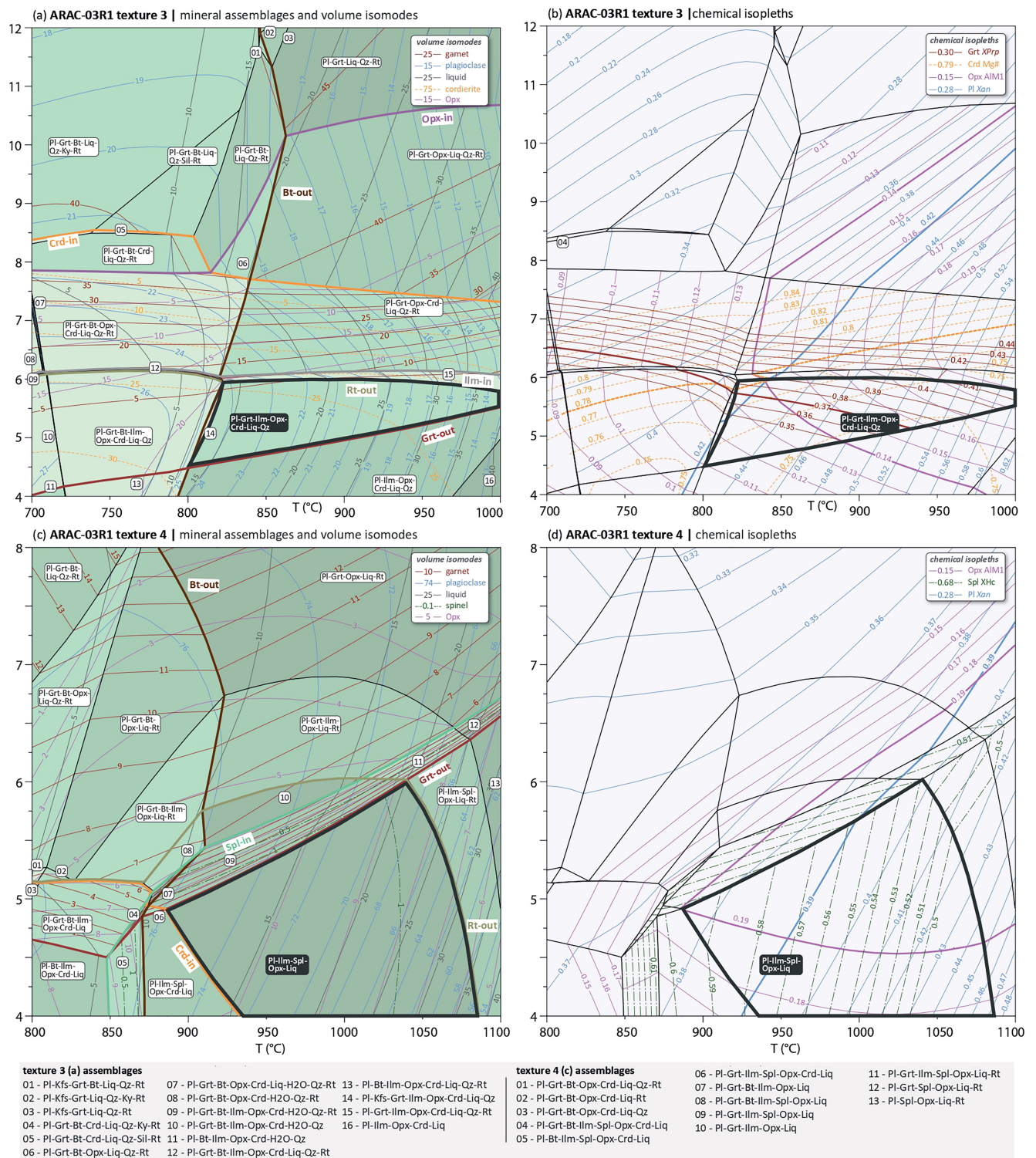


FIGURE 11 | Isochemical phase diagrams for ARAC-03R1 *Texture 3* (a,b) and *Texture 4* (c,d): (a) *Texture 3* mineral assemblages and volume isomodes with main phase reactions; (b) *Texture 3* chemical isopleths; (c) *Texture 4* mineral assemblages and volume isomodes with main phase reactions; (d) *Texture 4* chemical isopleths. In parts (a) and (c), darker and lighter shades of green represent high and low variance fields, respectively.

are generally colourless, homogeneous, spherical multifaceted ('soccer ball') grains. The average diameter is 125 µm, and the length:width ratio is 1:1 for most crystals. Back-scattered electron (BSE) images show mostly inclusion-free and homogeneous crystals. CL images highlight homogeneous grey/dark luminescent grains with very incipient oscillatory zoning in the rims

(Figure 12a). In the crystals with core/rim textures, the rims show brighter luminescence and prominent oscillatory zoning, and the cores are characterized by dark grey luminescence (Figure 12a). REE patterns, normalized to chondrite, are similar across the analysed spots. They display a depletion in LREE, a distinct negative anomaly in Eu and enrichment in HREE

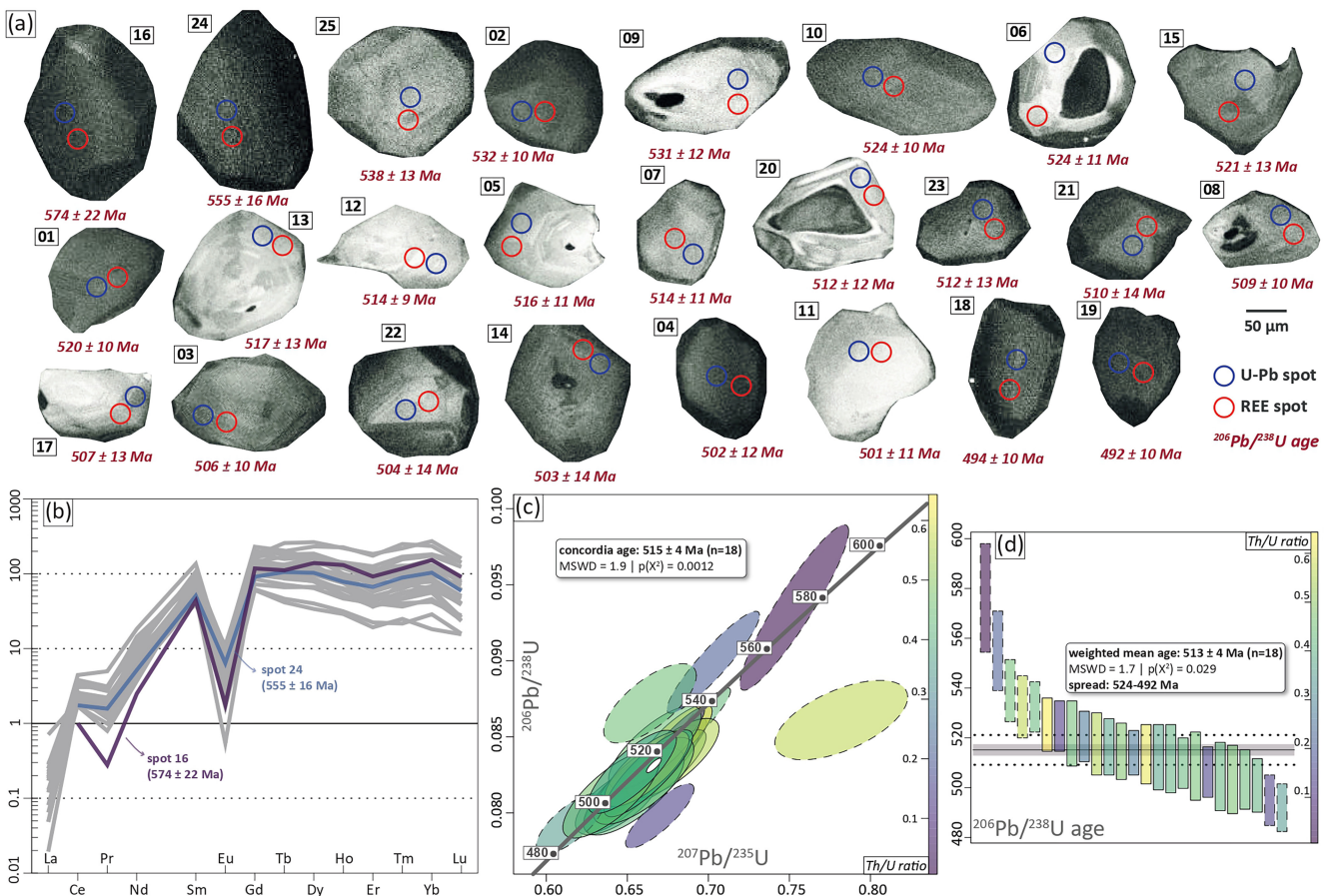


FIGURE 12 | Zircon geochronological results for sample ARAC-01B: (a) cathodoluminescence zircon imaging with spot location examples; (b) REE profile; (c,d) U-Pb zircon concordia and weighted mean ages. Dashed strokes are discordant ages, not used in calculations and plotted for reference only. 2σ errors reported.

(Figure 12b). Th/U ratios for concordant analyses range from 0.13 to 0.62. Higher Th/U values (0.54–0.62) are concentrated in the brighter luminescent rims around the darker cores. Except for one older zircon (zircon 16–574 ± 22 Ma), all concordant dates (<2% discordance) range from 532 ± 10 to 492 ± 10 Ma. The calculated concordia age (Figure 12c) yields 515 ± 4 Ma ($n = 18$, MSWD = 1.9, $p[\chi^2] = 0.0012$), and the calculated $^{206}\text{Pb}/^{238}\text{U}$ weighted mean age is 513 ± 4 Ma ($n = 18$, MSWD = 1.74, $p[\chi^2] = 0.029$) (Figure 12d). Both concordia and weighted mean ages were calculated after excluding dates with discordance of more than 2% and three dates were considered outliers.

The analysed garnet grains are idioblastic to subidioblastic and show general homogeneous major elements composition (see Data S7). The REE profile of a representative garnet crystal displays a bell-shaped Lu distribution (from 15.5 ppm in the core to 1.1 ppm in the rim, Figure 13a); a similar pattern for Yb (core to rim from 93 to 8 ppm, not plotted). Garnet Hf contents show slightly lower values in the core, ranging from 0.16 ppm in the core to 1.6 ppm in the rim (Figure 13a), and Sm is relatively homogeneous in the core-to-rim profile, with an average content of 0.26 ppm (Figure 13a). Chondrite-normalized REE plots show a general depletion of light rare-earth elements (LREE) and a more pronounced Eu negative anomaly in the core when compared with the mantle and rim, and heavy rare-earth elements (HREE) depletion from core to rim (Figure 13b).

Lu-Hf and Sm-Nd isotope data are shown in Table 2. A four-point Lu-Hf isochron yielded a 528 ± 3 Ma age (MSWD = 0.4) with initial $^{176}\text{Hf}/^{177}\text{Hf}$ of $0.282207 \pm 14\text{e-}6$ (Figure 13c). A two-point isochron using the whole-rock and garnet 4 (G4) analysis (G4 was excluded from calculation of the four-point isochron) points to a maximum garnet age of 534 ± 3 Ma (Figure 13c). The Sm-Nd isochron age is 492 ± 2 Ma (MSWD = 0.91) with initial $^{143}\text{Nd}/^{144}\text{Nd}$ of $0.5101604 \pm 28\text{e-}6$ (Figure 13d).

7.2 | In-Source Leucosome With Garnet + Cordierite + Sillimanite + Spinel (ARAC-02C)

The zircon grains from sample ARAC-02C are grouped into two populations based on textural features (Data S7). *Population 1* comprises mostly brownish prismatic crystals with dark cores and a distinct rough surface. Average crystal length is 250 μm, ranging from 100 to 400 μm, with a length:width ratio of 2.5:1. CL images of *Population 1* are mostly homogeneous with moderate to dark luminescent crystals. Some grains show heterogeneous cores with discrete oscillatory zoning, including dark luminescent prismatic shapes, commonly rimmed by thin bright luminescent overgrowths (Figure 14a). Within this population, two distinct REE signatures are discernible in chondrite-normalized diagrams. One group exhibits enriched LREE, a moderate positive Eu

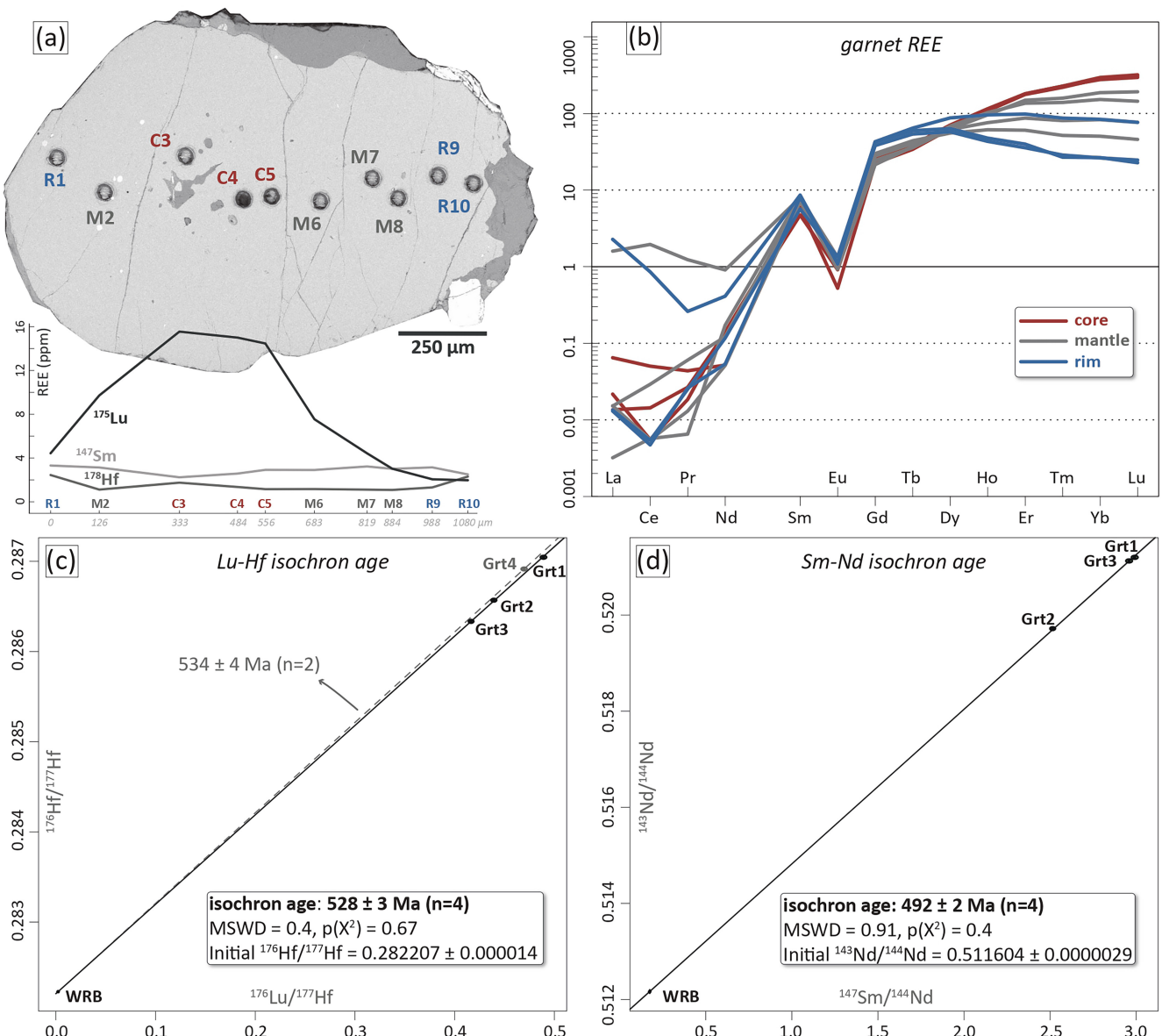


FIGURE 13 | Garnet geochronological results for sample ARAC-01B: (a,b) Garnet ^{175}Lu , ^{178}Hf and ^{147}Sm core to rim and REE profiles (see text for description); (c,d) garnet Lu–Hf and Sm–Nd isochron plots considering garnet and whole-rock aliquots (Grt and WRB, respectively). 2σ errors reported.

anomaly, and a steep HREE pattern. The other group is characterized by depleted LREE, the absence of an Eu anomaly, and enriched HREE (Figure 14b,c). Th/U ratios are very low (<0.012) for both groups (Figure 14d). In terms of dates, there is no distinction between the two groups, and individual spots are spread from 576 to 516 Ma, but the majority of dates are concentrated around 556 ± 8 and 531 ± 9 Ma (Figure 14e). Three younger dates (<520 Ma) within this population are associated with rim overgrowths (Figure 14a).

The second population (*Population 2*) includes colourless to pale yellow prismatic crystals with clean surfaces and minor spherical subrounded crystals (Data S6). The length of the prismatic crystals ranges from 100 to 450 μm, and the length:width ratio is up to 6:1 in bigger crystals. Spherical crystals have an average diameter of 125 μm. CL images show homogeneous dark to moderate luminescence as in *Population 1*, with absence of oscillatory zoning (Figure 14f). The REE chondrite-normalized diagram for this

population exhibits patterns similar to those of the zircon grains from ARAC-01B, involving depleted LREE, a prominent negative Eu anomaly and enriched but flat HREE. Th/U ratios range from 0.29 to 0.50. Most of the concordant analyses range from 516 ± 9 to 491 ± 8 Ma. The calculated concordia age is 497 ± 2 Ma ($n=11$, MSWD = 1.2, $p[\chi^2] = 0.27$) and the calculated $^{206}\text{Pb}/^{238}\text{U}$ weighted mean age is 497 ± 3 Ma ($n=11$, MSWD = 0.92, $p[\chi^2] = 0.51$).

8 | Discussion

8.1 | Regional Metamorphism

P-T estimates from three closely spaced samples along a roadcut (Figure 2c) define a coherent clockwise metamorphic trajectory for the NCV, characterized by a near-peak pressure conditions followed by near-isothermal decompression and overprinting by localized contact metamorphism.

TABLE 2 | Lu-Hf and Sm-Nd isotopic data (ARAC-01B).

Lu-Hf analysis						
Fraction	Lu (ppm)	Hf (ppm)	$^{176}\text{Lu}/^{177}\text{Hf}$	$\pm 2\sigma$	$^{176}\text{Hf}/^{177}\text{Hf}$	$\pm 2\sigma$
Garnet 1 (G1)	5.062	1.469	0.489108	0.002446	0.287045	0.000015
Garnet 2 (G2)	4.719	1.525	0.439317	0.002197	0.286569	0.000015
Garnet 3 (G3)	4.615	1.573	0.416488	0.002082	0.286334	0.000015
Garnet 4 (G4)	4.907	1.483	0.469688	0.002348	0.286915	0.000015
Whole-rock (WRB)	0.068	4.521	0.002281	0.000011	0.282229	0.000014
Sm-Nd analysis						
Fraction	Sm (ppm)	Nd (ppm)	$^{147}\text{Sm}/^{144}\text{Nd}$	$\pm 2\sigma$	$^{143}\text{Nd}/^{144}\text{Nd}$	$\pm 2\sigma$
Garnet 1 (G1)	1.869	0.379	2.991468	0.01496	0.5212	0.00003
Garnet 2 (G2)	1.806	0.435	2.51483	0.01257	0.519717	0.000028
Garnet 3 (G3)	1.603	0.328	2.958921	0.01479	0.521126	0.00003
Whole-rock (WRB)	4.545	15.714	0.174915	0.00087	0.512166	0.000027

Near-peak pressure conditions were constrained at 770°C–830°C and 6.5–10.5 kbar, considering the mineral paragenesis of plagioclase, K-feldspar, garnet, sillimanite, biotite, ilmenite, quartz and liquid in the cordierite-garnet granulite (ARAC-01B, Figure 10a). The P-T estimates obtained in this study are similar to the published near-peak temperature estimates for other granulitic rocks within the Nova Venecia complex (Munhá et al. 2005; Richter et al. 2016, Figure 15a) but suggest slightly higher pressures (Figure 15b). Pressure conditions up to 10.5 kbar have been calculated for (\pm sillimanite)-garnet-bearing granites from large peraluminous batholiths in the hot anatetic domain (Melo et al. 2017b). Nonetheless, most of the available near-peak P-T constraints for the cordierite-bearing high-grade rocks of the Araçuaí-Ribeira orogenic system, including the Nova Venecia complex, consider cordierite (\pm spinel) as a stable phase under near-peak metamorphic conditions (e.g., Munhá et al. 2005; Wisnioski et al. 2020, Figure 15a), which could explain the lower pressure estimates.

Conversely, our textural and chemical evidence from the studied cordierite-bearing paragneisses indicate that cordierite (\pm spinel) replaces near-peak pressure assemblages such as garnet and sillimanite (Figures 5f–i, 6 and 7). The metamorphic reactions $\text{biotite} + \text{garnet} + \text{sillimanite} \rightarrow \text{spinel} + \text{cordierite} + \text{K-feldspar} + \text{melt}$ and $\text{garnet} + \text{sillimanite} \rightarrow \text{cordierite} + \text{spinel} + \text{quartz}$ can indeed account for the observed textures. Both reactions have moderate slopes in the P-T space, with the latter displaying a shallower gradient (Dasgupta et al. 1997; Spear et al. 1999; Shabeer et al. 2002). These textures are observed in both samples ARAC-01B (*Texture 1*) and ARAC-02B (*Texture 2*). P-T estimates using the composition from sample ARAC-02B suggest metamorphic conditions at lower pressures, ~4.5 to 5.5 kbar and temperatures in the range of ~770°C–870°C (Figure 10c), consistent with a stage of near-isothermal decompression following peak pressure conditions.

Additional reaction textures, such as xenoblastic/poikiloblastic garnet being replaced by subidioblastic orthopyroxene, quartz,

plagioclase, cordierite and K-feldspar are also observed in the hornfels (ARAC-03R1—*Texture 3*, Figure 9a–f). This texture was modelled using the X-ray compositional map and the mineral assemblage of plagioclase, garnet, biotite, orthopyroxene, cordierite, ilmenite, quartz and liquid representing the local equilibria (Figure 11a). The stability field of this mineral assemblage indicates P-T conditions at around 4.5–6 kbar and temperatures exceeding 800°C (Figure 11a), further supporting a stage of decompression following peak pressure conditions. Forward thermodynamic modelling of other granulitic samples from the Nova Venecia complex also reinforces the interpretation of a near-isothermal decompression path during the evolution of these rocks (Richter et al. 2016). In contrast, Wisnioski et al. (2020) interpret replacement reactions, including the consumption of garnet and sillimanite to produce cordierite and spinel, as a result of an isobaric heating stage associated with the intrusion of the gabbroic stock. Indeed, the modelled P-T conditions for the general texture of the hornfels (*Texture 3*, Figure 11a–b) suggest decompression accompanied by minor heating. However, the other modelled samples (ARAC-01B and ARAC-02B) are more consistent with a near-isothermal decompression trajectory.

Forward thermodynamic modelling based on bulk composition from samples ARAC-01B, ARAC-02B and ARAC-03R1 (*Texture 3*) yielded coherent P-T estimates indicating near-peak pressure conditions, followed by a near-isothermal decompression in samples located away from the intrusion (Figure 10a–d), and decompression accompanied by minor heating in the sample next to the intrusion (Figure 11a–b). These P-T paths are primarily constrained by the stability field of the observed mineral assemblage and are consistent with measured mineral volume isomodes and chemical isopleths.

8.2 | Contact Metamorphism

Local textures suggesting the transformation of orthopyroxene into spinel involving plagioclase (*Texture 4*, Figure 9g–i)

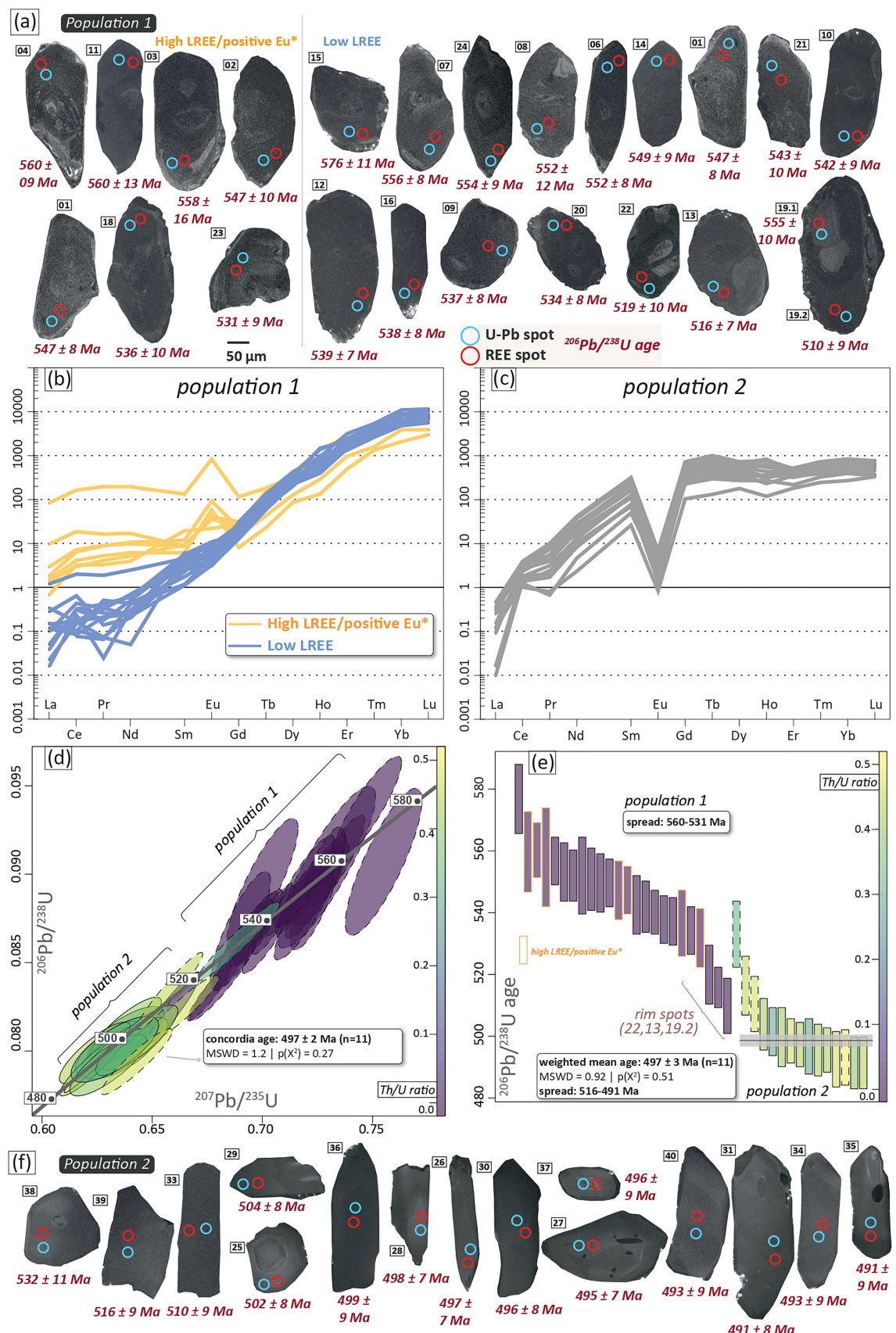


FIGURE 14 | Zircon geochronological results for Sample 02B Populations 1 and 2 (see text for description). (a) Population 1 cathodoluminescence zircon imaging with spot location examples from both high LREE/positive Eu and low LREE groups; (b,c) Populations 1 and 2 zircon REE profiles respectively; (d) Population 2 U–Pb zircon concordia age; (e) Populations 1 and 2 weighted mean ages/spread; dashed strokes are discordant ages, not used in calculations and plotted for reference only. (f) Population 2 cathodoluminescence zircon imaging with spot location. 2σ errors reported.

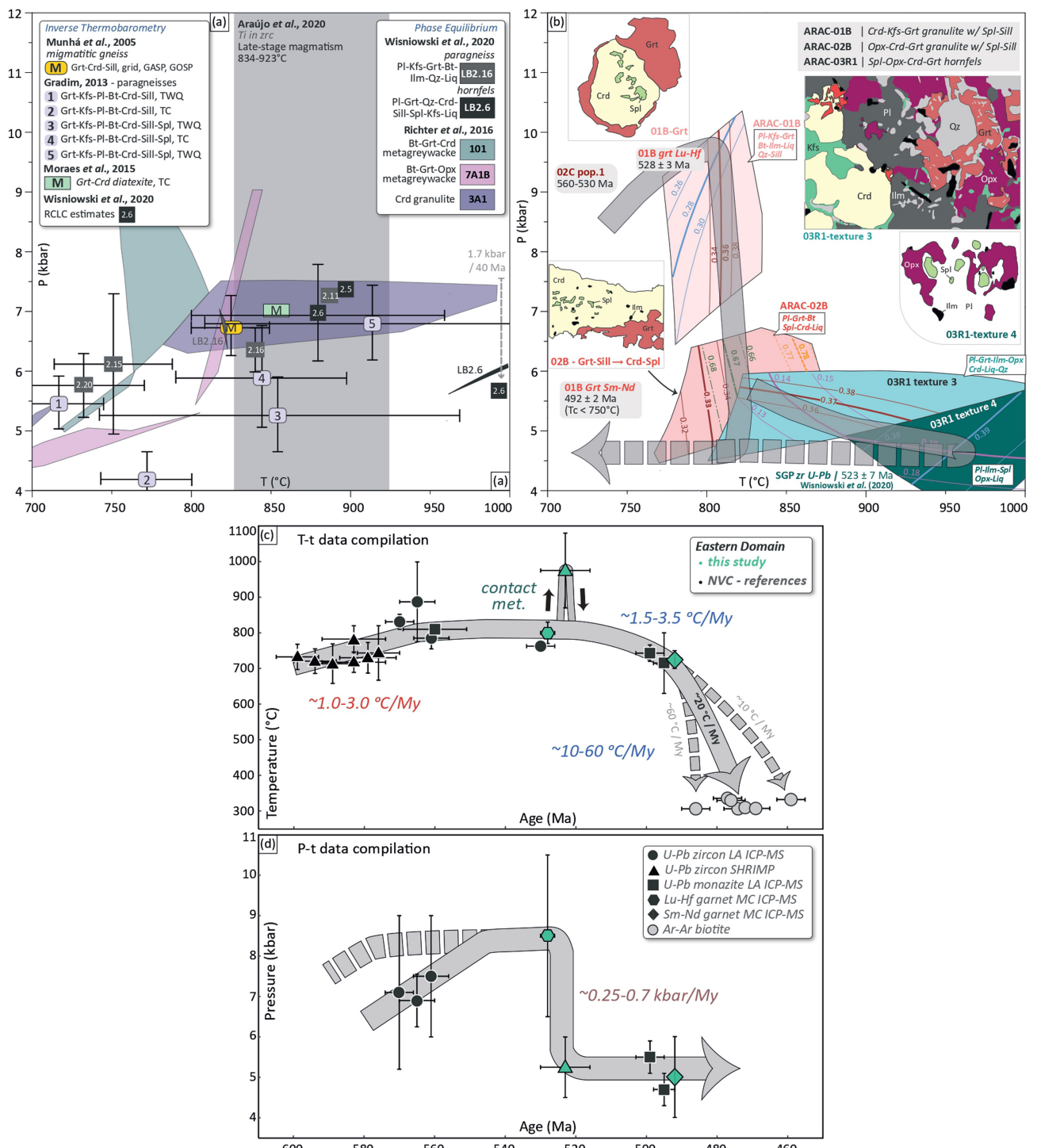


FIGURE 15 | (a) Compiled P-T estimates for the Araçuaí orogen granulites including data from Munhá et al. (2005), Gradim et al. (2014), Moraes et al. (2015), Richter et al. (2016), Araújo et al. (2020) and Wisniowski et al. (2020); (b) P-T-t diagram with thermodynamic results from this work, including main textures, correlated ages, and the interpreted isothermal decompression path and local contact metamorphism; (c,d) T-t and P-t plots from Araçuaí orogen Eastern Domain, including data from this work, U-Pb ages coupled with Ti-in-zircon thermometry (Cavalcante et al. 2018), P-T estimates coupled with zircon and monazite dating from Richter et al. (2016) and Melo et al. (2017a), zircon U-Pb SHRIMP from Wisniowski et al. (2020) and Ar-Ar cooling ages from Vauchez et al. (2019).

are observed in the hornfels next to the gabbro intrusion (Figures 2c and 4) and represent only minor components in the overall rock volume (Figure 8e,f). The P-T constraints for these textures suggest heating to conditions of 870°C–1080°C at ~4–6 kbar (Figure 11c,d). The isochemical phase diagram

(Figure 11c) also predicts orthopyroxene consumption and spinel formation during heating above 900°C at lower pressures, supporting this interpretation. Patchy compositional zoning observed in the reacting minerals, particularly prominent in plagioclase (Figure 9h), indicates partial equilibration and may

be attributed to chemical potential gradient and diffusion occurring during either heating or cooling pathways. However, field-based observations, petrographic features, previous studies (Wisniowski et al. 2020) and modelled mineral assemblage, volumes and chemistry corroborate with the hypothesis of heating under low pressures (5–6 kbar). The temperature conditions exceeding 850°C–900°C identified in domains within the hornfels are thought to be confined to the immediate vicinity of the gabbro aureole, that is, <2 m from the contact (see Figure 2c). P-T estimates derived from *Texture 3* in the hornfels (Figure 11c,d) also suggest heating at relatively low pressures following a decompression event. The argument of localized overprinting by contact metamorphism is supported by (i) the presence of diffusive contacts between the intrusive gabbro and the host granulites, indicating that the host rocks were partially molten (at suprasolidus conditions) at the time of intrusion; (ii) the restricted spatial distribution of UHT assemblages within the hornfels, such as *Texture 4*; and (iii) the absence of heating-related reactions or textures in other studied samples across the outcrop. This interpretation contrasts with the proposition of Wisniowski et al. (2020) and implies that advective heating from high-temperature magmas had a limited impact on the thermal history of the Nova Venecia complex, at least in the investigated region.

8.3 | Petrochronological Constraints: The P-T-t History of the Hot Anatetic Domain

Timing constraints on the metamorphic history of orogenic rocks provide empirical data to understand the duration of orogenic processes (e.g., Engi et al. 2017), including the geodynamic evolution of hot orogens. In this study, U-Pb and REE zircon data and Lu-Hf and Sm-Nd garnet dating are used to constrain the timing of different metamorphic stages along the P-T evolution for the studied samples. The oldest U-Pb dates observed in this work vary from ~575 to 540 Ma (Figure 14) and were obtained in zircon grains showing homogeneous texture to subtle oscillatory zoning and generally low luminescence (Figures 12a and 14a). These zircon grains are mostly represented by *Population 1* from a leucosome (ARAC-02C; Figure 14), which yield low Th/U ratios (<0.01) and steep HREE patterns in chondrite-normalized diagrams (Figure 14b). These geochemical signatures are compatible with the growth of metamorphic zircon within an assemblage rich in light and middle rare-earth elements (L-MREE) such as monazite (Rubato et al. 2009; Rubato 2017). Two groups of zircon in *Population 1* can be distinguished based on their LREE contents and Eu anomaly but share an enriched HREE pattern (Figure 14b). The first one shows an enriched LREE pattern and a pronounced positive Eu anomaly. Enriched LREE suggests zircon growth at the expense of monazite, whereas the positive Eu anomaly indicates consumption of plagioclase and/or alkali feldspar at upper amphibolite-facies conditions (Rubato 2017; Yakymchuk 2023). Conversely, the second group shows a typical REE pattern for metamorphic zircon growing in an assemblage rich in monazite, including depleted LREE, a positive Ce anomaly, a steep Pr-Lu pattern and the absence of an Eu anomaly (Rubato 2017). Although the LREE contents in these two groups indicate opposite growth relationships with monazite, the shared enriched HREE signatures suggest zircon

growth before garnet crystallization, likely during prograde metamorphism.

No distinguishable U-Pb dates are observed within these two groups (Figure 14e). In fact, the distribution of older U-Pb dates (*Population 1*, ARAC-02C and a few grains in ARAC-01B) is spread along the concordia (Figure 14d) and can be interpreted as either continuous growth of zircon for 30–40 My or lead-loss from grains crystallized at around 580–570 Ma. Either explanation implies the maintenance of high-temperature conditions (>750°C–800°C) for tens of millions of years. Similar or longer timescales have been recognized in hot orogens elsewhere (Herman and Rubatto 2003; Harley 2016; Clark et al. 2011, 2015, 2024). The available U-Pb data from the Nova Venecia complex indicate a peak of metamorphic zircon and monazite crystallization at around 580–560 Ma but also show a spread of dates down to 540 Ma along the concordia (Richter et al. 2016 and references therein). The interpretation of the age peak around 570 Ma as the regional metamorphic peak for the hot anatetic domain is common in the literature (e.g., Pedrosa-Soares et al. 2011; Gradim et al. 2014; Richter et al. 2016); however, the temperature-time diagram based on the available data (Figure 15c) suggests a later metamorphic peak at around 540–530 Ma. We interpret the older U-Pb metamorphic dates for zircon and monazite (spreading from 580 to 540 Ma) as representative of crystallization under prograde metamorphism at upper amphibolite conditions, associated with muscovite breakdown incongruent melting reaction (e.g., Yakymchuk 2023) during 580–570 Ma (Figure 15b). This interpretation is corroborated by the enriched HREE patterns of the dated older zircon grains in the leucosome (*Population 1*, ARAC-02C) and the large volume of peraluminous S-type granitoids within the hot anatetic domain yielding crystallization ages of 580–560 Ma (e.g., Pedrosa-Soares et al. 2011; Richter et al. 2016). Therefore, the spreading of dates along the concordia (Figure 14d) likely represents lead-loss during long-lasting high-temperature conditions.

The Lu-Hf garnet age of 528 ± 3 Ma obtained in this study (Figure 13c) also supports a later timing for the metamorphic peak in the hot anatetic domain (Figure 14d). The simple bell-shaped Lu distribution within the analysed garnet grains and REE pattern from core to rim (Figure 13a,b) can be explained by Rayleigh fractionation during a single, continuous growth event of garnet (e.g., Smit et al. 2013, 2024). The presence of quartz, K-feldspar, multiphase quartz-feldspathic and sillimanite inclusions in the core and inner rim of the analysed grains (Figures 5f, 6a and 13a) indicates garnet growth during near-peak conditions in the presence of melt. However, forward thermodynamic modelling predicts 20% volume of garnet in the modelled rock before reaching the constrained near-peak conditions (Figure 10a). The forward thermodynamic modelling also indicates rapid increase in garnet volume after reaching the K-feldspar stability field (Figure 10a). Overstepping reactions and late growth of garnet at suprasolidus conditions may explain the discrepancies between garnet core inclusions and the predictions from the forward thermodynamic modelling. Considering that, the obtained Lu-Hf age is interpreted as the timing of garnet growth under prograde to near-baric peak conditions (e.g., Anczkiewicz et al. 2014; Smit et al. 2024), constrained at temperatures of 770°C–850°C and pressures of 6.5–10 kbar (Figures 10a and 15b).

Metamorphic ages around 530 Ma are uncommon for the Araçuaí orogen, highlighting a notable gap in the zircon and monazite age records (e.g., Richter et al. 2016; Melo et al. 2017a, 2017b). Only a limited number of concordant U–Pb zircon dates have been documented for the crystallization of peraluminous leucogranites within the 540–525 Ma interval (Petitgirard et al. 2009; Pedrosa-Soares et al. 2011; Richter et al. 2016), along with a few U–Pb zircon and monazite dates interpreted as recording cryptic anatetic events (Melo et al. 2017a, 2017b). A less precise Sm–Nd garnet age of 538 ± 35 Ma is also reported for a migmatite sample in the hot anatetic domain (Brueckner et al. 2000). The apparent inconsistency between the newly obtained Lu–Hf garnet age and the available metamorphic ages for the hot anatetic domain can be attributed to the lack of studies employing multimineral geochronology and different isotopic systems. Based on the interpretation that the studied rocks reached near-peak conditions around 530 Ma, we propose that prograde metamorphism in the hot anatetic domain evolved continuously from at least 580–570 Ma to 530 Ma. This evolution was likely driven by orogenic thermal maturation due to the redistribution of HPEs throughout the crust (e.g., Smithies et al. 2015). During this time interval, the heating rate was modest, increasing by $\sim 1^\circ\text{C}$ – 3°C per million years, from about 700°C to 800°C–850°C (Figure 15c).

After reaching peak pressure conditions, the studied rocks followed a near-isothermal decompression path, recorded by the replacement of garnet (\pm sillimanite) by cordierite, spinel \pm orthopyroxene (Figures 6, 7 and 9). The P–T conditions after decompression are constrained at approximately 5 kbar and 770°C–870°C from sample ARAC-02B (Figure 10c,d). Zircon grains causing pleochroic halos in cordierite (Figures 5f and 6d) indicate cordierite growth around residual zircon or paragenetic growth of zircon and cordierite. The qualitative correlation between U–Pb dates and decompression reactions (e.g., Degeling et al. 2001) is precluded by the zircon REE signatures (Figure 12b). These zircon grains (ARAC-01 and *Population 2* in ARAC-02B) show a homogeneous chondrite-normalized REE pattern, featuring a prominent negative Eu anomaly and flat HREE (Figures 12b and 14c), along with high Th/U ratios (Figures 12d and 14c). These signatures indicate zircon growth in the presence of garnet, consistent with granulite-facies zircon grains formed from anatetic melts (Rubato 2017). Individual U–Pb zircon dates for the sample ARAC-01B and *Population 2* from sample ARAC-02B vary from ~ 532 to 491 Ma (Figures 12d, 14e); however, concordia and weighted mean ages from both samples yield approximately 510 to 500 Ma (Figures 12c,d and 14d,e). As discussed above, the spreading of U–Pb dates along the concordia may represent continuous growth or lead-loss processes. Considering the consistency of the REE signatures in zircon and their correlation with zircon growth in the presence of garnet, we interpret the timing of zircon growth at circa 530 Ma, with spreading of U–Pb dates associated with lead-loss at ~ 500 Ma, before cooling. Therefore, the concordia and weighted mean ages do not represent crystallization ages but rather a minimum age for cooling to subsolidus conditions.

The thermal influence of gabbroic rock emplacement into granulitic rocks is indicated by the presence of local atoll

orthopyroxene textures (*Texture 4*). These textures are characterized by orthopyroxene surrounding plagioclase in the mantle and spinel cores (Figure 9g–i) within hornfels near the intrusion (Figure 2c). The orthopyroxene formation in these rocks is interpreted to be a result of decompression reactions involving consumption of garnet. Therefore, the subsequent consumption of orthopyroxene and the development of atoll textures are thought to have occurred after the decompression event. The P–T conditions for the atoll texture formation are constrained at approximately 5 kbar and temperatures above 900°C (Figure 11c). The timing for the emplacement of the gabbroic stock and contact metamorphism is constrained by the crystallization age for the gabbro norite (523 ± 7 Ma, Wisnioski et al. 2020).

Concordia and weighted mean zircon ages around 510–500 Ma (Figures 12c,d and 14e), coupled with the Sm–Nd garnet age of 492 ± 2 Ma (Figure 13d), reasonably constrain the timing of final cooling to below 750°C (Figure 15b,c). Further cooling is recorded by Ar–Ar ages that constrain temperatures below 300°C at approximately 480–460 Ma (Vauchez et al. 2019).

8.4 | Geodynamic Implications

The evolution of the Araçuaí orogen spanned over 120 million years of magmatism, metamorphism and deformation (Alkmim et al. 2006; Pedrosa-Soares et al. 2011), reflecting a long-lived history that included crustal thickening, orogenic thermal maturation and orogenic collapse. Crustal thickening of at least 60–70 km is inferred for this orogen, based on the current crustal thickness of ~ 40 km (Assumpção et al. 2013) and palaeopressures of 7 to 10 kbar, calculated from currently exposed rocks (Figures 10a and 15a,b; Vauchez et al. 2019). The onset of crustal thickening in the Araçuaí orogen remains a matter of debate (e.g., Gradim et al. 2014; Cavalcante et al. 2019; Fossen et al. 2020). However, the crystallization of peraluminous granites around 600–590 Ma (e.g., Gradim et al. 2014; Cavalcante et al. 2018) implies that orogenic thickening occurred earlier than 620 Ma (Vauchez et al. 2019; Cavalcante et al. 2019). A plateau-like evolution for the internal domain of the orogen has been proposed by Fossen et al. (2017) and further developed by Cavalcante et al. (2019, 2021). In this model, the authors suggest the formation of an orogenic plateau following approximately 500 km of crustal convergence (Cavalcante et al. 2019). The thermal maturation of the overthickened crust, driven by heating from HPEs (e.g., England and Thompson 1984; Clark et al. 2015), would have raised the temperature of the middle crust above the solidus, resulting in the generation of migmatites and voluminous crustal melts at 600–570 Ma (Cavalcante et al. 2021; Schannor et al. 2021). Later collapse of the orogenic plateau is constrained by near-isothermal decompression (Richter et al. 2016; Schannor et al. 2021, Figure 15a,b) and high-temperature magmatism, including charnockitic magmas and mantle-derived gabbroic melts, at approximately 520–500 Ma (e.g., De Campos et al. 2016; Araujo et al. 2020). Although the general evolution associated with crustal thickening and orogenic collapse is reasonably well constrained for the Araçuaí orogen (e.g., Pedrosa-Soares et al. 2011; Alkmim et al. 2017; Cavalcante et al. 2021), the data presented in this study provide new insights into the geodynamic evolution of the hot anatetic domain.

The available P-T-t data, along with our new findings, indicate burial and heating of the sedimentary sequence in the hot anatetic domain (Nova Venecia complex) to conditions above the solidus before 600 Ma (Figure 15c). A heating rate of approximately $1^{\circ}\text{C}/\text{My}$ – $3^{\circ}\text{C}/\text{My}$ is inferred from the compiled data for the period between 600 and 560 Ma (Figure 15c). It is hypothesized that burial and heating until 570–580 Ma is related to crustal thickening and thermal maturation driven by radiogenic heat from anomalous concentrations of HPEs inherited from the Nova Venecia metasedimentary rocks (Schannor et al. 2021). The maintenance of temperatures around 800°C – 850°C in the plateau core middle crust from 570–560 Ma to ~530 Ma was possibly associated with a blanket effect caused by the redistribution of HPEs in the middle crust due to the emplacement of large volumes of peraluminous granitoids (Smithies et al. 2011; Cavalcante et al. 2021). According to Cavalcante et al. (2021), these granitoids were emplaced in the middle crust (~25–30 km deep) not far from their sources and evolved as a partially molten (mush-like) tabular anatetic body between at least 600 and 570 Ma, with limited vertical transport. Calculations of radiogenic heat production of these anatetic melts, based on the bulk-rock concentrations of U, Th and K from Cavalcante et al. (2021) and heat production rates from Ryback (1988), indicate heat production values higher than the average upper crust, with a median of $2.04 \mu\text{W/m}^3$ and anomalous values up to $14.62 \mu\text{W/m}^3$ (see Data S8). These data are consistent with the interpretation of long-lasting temperature conditions in the overthickened middle crust sustained by a single and evolving radiogenic heat source during the history of the orogenic plateau development from approximately 600 to around 530 Ma (Cavalcante et al. 2021). The U-Pb data and P-T estimates presented by Melo et al. (2017a, 2017b) for the evolution of the hot anatetic domain are also consistent with this interpretation.

The Lu-Hf garnet age of 528 ± 3 Ma is considered a minimum age for the peak conditions in the hot anatetic domain. Around this time, the thermally evolved orogenic plateau reached a critical mechanical state that enabled its collapse. Decoupling of the lithosphere and subsequent delamination are possible geodynamic processes that could account for this collapse (Vanderhaeghe 2012). P-T thermodynamic modelling of replacement textures (*Textures 1* and *2*) suggests that near-isothermal decompression occurred around 525 Ma at exhumation rates of ~0.25–0.7 kbar/My (Figure 15d). This near-isothermal decompression event is widely recognized within the internal domain (e.g., Richter et al. 2016; Melo et al. 2017a, 2017b; Schannor et al. 2021) and likely represents the record of the plateau collapse. The collapse of the orogenic plateau is also evidenced by extensional structures in the external domain (e.g., Alkmim et al. 2006) and widespread high-temperature magmatism in the internal domain between 530 and 490 Ma (De Campos et al. 2016; Araujo et al. 2020; Cavalcante et al. 2021; Temporim et al. 2023). A cause-and-effect relationship between this high-temperature magmatism and the orogenic/plateau collapse has been postulated, primarily associated with asthenospheric upwelling due to slab break-off (e.g., De Campos et al. 2016; Gradim et al. 2014) or mantle plumes (e.g., Serrano et al. 2018). However, the continuous thermal evolution of the orogenic plateau, as proposed in this study, does not require additional geodynamic processes

such as slab break-off or mantle plumes to explain this late high-temperature magmatism. Instead, our preferred model attributes high-temperature melting of the lower crust and mantle during the late orogenic stage to extreme thermal maturation of the crust, followed by adiabatic melting after lithospheric delamination.

Low-pressure/high-temperature metamorphism in the hot anatetic domain during the late stage of the orogenic evolution (~520–490 Ma) has been used to support tectonic models associated with episodic heating (e.g., Melo et al. 2017a, 2017b; Serrano et al. 2018). However, the local thermal impact of the gabbroic intrusion within the Nova Venecia complex in the studied region indicates that the advective heating from the high-temperature magmatism had a minor influence on the heat budget of the hot anatetic domain, even during the late-stage evolution of the orogen. Rather than a new metamorphic cycle driven by additional advective heating, the late orogenic stage (or collapse stage) is characterized by the waning of middle crustal flow, extensional deformation in the mid-upper crust (e.g., Alkmim et al. 2006; Schannor et al. 2021) and vertical to orogen-parallel magma transport (e.g., Temporim et al. 2023). Cooling of the orogen proceeds at slow rates ($\sim 1.5^{\circ}\text{C}/\text{My}$ – $3.5^{\circ}\text{C}/\text{My}$) during the collapse stage (~490–520 Ma), but rapid cooling ($\sim 10^{\circ}\text{C}/\text{My}$ – $60^{\circ}\text{C}/\text{My}$) is observed after crystallization of the high-temperature magmatism (<490 Ma) (Figure 15c; Vauchez et al. 2019).

9 | Conclusions

In this contribution, we present a comprehensive metamorphic study for high-grade metamorphic rocks from the hot anatetic domain of the Araçuaí orogen. Our study includes thermodynamic modelling, Lu-Hf and Sm-Nd garnet dating, and U-Pb and REE zircon data. Integrating these data with existing geological and geochronological information from the Araçuaí orogen allows us to propose a continuous thermal evolution for the internal domain of the orogen.

According to our model, the internal domain evolved as an orogenic plateau, formed after contractional deformation and thickening driven by more than 500 km of crustal convergence. This crustal convergence likely began earlier than 620 Ma. The plateau-like evolution, characterized by the lateral flow of partially molten middle crust towards the foreland domains, started at approximately 600 Ma and continued until 540–530 Ma. Thermal evolution of the plateau was primarily controlled by inherited HPEs within the thickened crust and redistribution of these elements after crustal melting. Peak conditions, approximately 800°C and 9–10 kbar, were achieved at circa 530 Ma. The extreme thermal maturation in the overthickened crust eventually led to the destabilization and collapse of the plateau.

We interpret the decoupling in the lithosphere and lithospheric delamination as the main geodynamic processes responsible for the plateau's collapse. This collapse induced near-isothermal decompression in the core of the plateau and high-temperature melting of the lower crust and mantle around 520–510 Ma. Low cooling rates were observed during collapse and late-stage

high-temperature magmatism. Throughout the evolution of the orogenic plateau, the middle to lower crust levels remained under suprasolidus conditions for nearly 100 My (from ~600 to 510 Ma). Contact metamorphism driven by the emplacement of high-temperature magmas was localized and apparently did not significantly influence the heat budget of the hot anatetic domain, at least in the studied region. After the collapse stage and crystallization of the high-temperature magmas, the collapsed orogen cooled rapidly, with cooling rates of ~20°C per million years.

Acknowledgements

We would like to acknowledge FAPESP (grants #2016/06114-6, #2017/003528-8, #2018/06011-8 and #2021/00967-5) and CNPq (grant #404767/2016-8) for financial support. V.T.M. acknowledges CNPq for research fellowship ‘Bolsa Produtividade em Pesquisa’ (grant #314473/2021-1). We thank Charles Knaack, Chris Fisher and Chao Zhang for technical and laboratory support with clean lab and ICP-MS analyses at WSU RIGL. We fully appreciate the critical comments and suggestions from Chris Yakymchuk, Johann Diener and an anonymous reviewer that substantially improved our manuscript. Johann Diener and Richard White are acknowledged for editorial handling. The Article Processing Charge for the publication of this research was funded by the Coordenação de Aperfeiçoamento de Pessoal de Nível Superior - Brasil (CAPES) (ROR identifier: 00x0ma614).

Conflicts of Interest

The authors declare no conflicts of interest.

Data Availability Statement

The data that support the findings of this study are available from the corresponding author upon reasonable request.

References

- Alkmim, F. F., S. Marshak, and M. A. Fonseca. 2001. “Assembling West Gondwana in the Neoproterozoic: Clues From the São Francisco Craton Region, Brazil.” *Geology* 29: 319–322.
- Alkmim, F. F., S. Marshak, A. C. Pedrosa-Soares, G. G. Peres, S. Cruz, and A. Whittington. 2006. “Kinematic Evolution of the Araçuaí-West Congo Orogen in Brazil and Africa: Nutcracker Tectonics During the Neoproterozoic Assembly of Gondwana.” *Precambrian Research* 149: 43–64.
- Alkmim, F. F., M. Kuchenbecker, H. L. S. Reis, and A. C. Pedrosa-Soares. 2017. “The Araçuaí-Belt.” In *São Francisco Craton, Eastern Brazil*, edited by M. Heilbron, U. G. Cordani, and F. F. Alkmim, 255–276. Springer International Publishing.
- Almeida, F. F. M. 1967. *Origem e Evolução da Plataforma Brasileira*, 241. DNPM - Boletim 36p.
- Amaral, L., F. A. Caxito, A. C. Pedrosa-Soares, et al. 2020. “The Ribeirão da Folha Ophiolite-Bearing Accretionary Wedge (Araçuaí Orogen, SE Brazil): New Data for Cryogenian Plagiogranite and Metasedimentary Rocks.” *Precambrian Research* 336: 105522.
- Anczkiewicz, R., and M. F. Thirlwall. 2003. “Improving Precision of Sm–Nd Garnet Dating by H_2SO_4 Leaching: A Simple Solution to the Phosphate Inclusion Problem.” *Geological Society, London, Special Publications* 220: 83–91.
- Anczkiewicz, R., S. Chakraborty, S. Dasgupta, and D. Mukhopadhyay. 2014. “Timing, Duration and Inversion of Prograde Barrovian Metamorphism Constrained by High Resolution Lu-Hf Garnet Dating: A Case Study From the Sikkim Himalaya, NE India.” *Earth and Planetary Science Letters* 407: 70–81.
- Araujo, C., A. C. Pedrosa-Soares, C. Lana, et al. 2020. “Zircon in Emplacement Borders of Post-Collisional Plutons Compared to Country Rocks: A Study on Morphology, Internal Texture, Ue-Th-Pb Geochronology and Hf Isotopes (Araçuaí Orogen, SE Brazil).” *Lithos* 352–353: 105252.
- Assumpção, M., M. Feng, A. Tassara, and J. Julià. 2013. “Models of Crustal Thickness for South America From Seismic Refraction, Receiver Functions and Surface Wave Tomography.” *Tectonophysics* 609: 82–96.
- Bea, F. 2012. “The Sources of Energy for Crustal Melting and the Geochemistry of Heat-Producing Elements.” *Lithos* 153: 278–291.
- Beaumont, C., R. Jamieson, and M. Nguyen. 2010. “Models of Large, Hot Orogens Containing a Collage of Reworked and Accreted Terranes.” *Canadian Journal of Earth Sciences* 47: 485–515.
- Bento dos Santos, T. M., C. C. G. Tassinari, and P. Fonseca. 2015. “Diachronic Collision, Slab Break-Off and Long-Term High Thermal Flux in the Brasiliano–Pan-African Orogeny: Implications for the Geodynamic Evolution of the Mantiqueira Province.” *Precambrian Research* 260: 1–22.
- Brito-Neves, B. B., and U. G. Cordani. 1991. “Tectonic Evolution of South America During Late Proterozoic.” *Precambrian Research* 33: 23–40.
- Brito-Neves, B. B., M. C. Campos-Neto, and R. A. Fuck. 1999. “From Rodinia to Western Gondwana: An Approach to the Brasiliano–Pan African Cycle and Orogenic Collage.” *Episodes* 22: 155–199.
- Brown, M. 2007. “Crustal Melting and Melt Extraction, Ascent and Emplacement in Orogens: Mechanisms and Consequences.” *Journal of the Geological Society, London* 164: 709–730.
- Brueckner, H. K., D. Cunningham, F. F. Alkmim, and S. Marshak. 2000. “Tectonic Implications of Precambrian Sm–Nd Dates From the Southern São Francisco Craton and Adjacent Araçuaí and Ribeira Belts, Brazil.” *Precambrian Research* 99: 255–269.
- Campos Neto, M. C. 2000. “Orogenic Systems From Southwestern Gondwana: An Approach to Brasiliano–Pan African Cycle and Orogenic Collage in Southeastern Brazil.” In *Tectonic Evolution of South America*, edited by U. G. Cordani, E. J. Milani, a. Thomaz Filho, and D. A. Campos, 335–368. 31st International Geological Congress.
- Cavalcante, G. C. G., A. Vauchez, C. Merlet, M. Egydio-Silva, M. H. Bezerra de Holanda, and B. Boyer. 2014. “Thermal Conditions During Deformation of Partially Molten Crust From TitaniQ Geothermometry: Rheological Implications for the Anatetic Domain of the Araçuaí Belt, Eastern Brazil.” *Solid Earth* 5: 1223–1242.
- Cavalcante, C., M. H. Holland, A. Vauchez, and M. Kawata. 2018. “How Long Can the Middle Crust Remain Partially Molten During Orogeny?” *Geology* 46: 839–842.
- Cavalcante, C., H. Fossen, R. P. Almeida, M. H. Holland, and M. Egydio-Silva. 2019. “Reviewing the Puzzling Intracontinental Termination of the Araçuaí-West Congo Orogenic Belt and Its Implications for Orogenic Development.” *Precambrian Research* 322: 85–98.
- Cavalcante, C., V. T. Meira, N. Magalhães, M. H. Holland, and E. Oliveira. 2021. “The Role of Ediacaran Synkinematic Anatetic Rocks and the Late-Orogenic Charnockitic Rocks in the Development of the Hot Araçuaí Belt.” *Precambrian Research* 365: 106396.
- Chardon, D., D. Gapais, and F. Cagnard. 2009. “Flow of Ultra-Hot Orogens: A View From the Precambrian, Clues for the Phanerozoic.” *Tectonophysics* 477: 105–118.
- Clark, C., I. C. W. Fitzsimons, D. Healy, and S. M. Harley. 2011. “How Does the Continental Crust Get Really Hot?” *Elements* 7: 235–240.
- Clark, C., C. L. Kirkland, C. V. Spaggiari, C. Oorschot, M. T. D. Wingate, and R. J. Taylor. 2014. “Proterozoic Granulite Formation Driven by

- Mafic Magmatism: An Example From the Fraser Range Metamorphics, Western Australia." *Precambrian Research* 240: 1–21.
- Clark, C., D. Healy, T. Johnson, et al. 2015. "Hot Orogens and Supercontinent Amalgamation: A Gondwanan Example From Southern India." *Gondwana Research* 28: 1310–1328.
- Clark, C., M. Brown, B. Knight, T. E. Johnson, R. J. Mitchell, and S. Gupta. 2024. "Ultraslow Cooling of an Ultrahot Orogen." *Geology* 52: 880–884.
- Collins, W. J. 2002. "Hot Orogens, Tectonic Switching, and Creation of Continental Crust." *Geology* 30: 535–538.
- Dasgupta, S., J. Ehl, M. M. Raith, P. Sengupta, and P. Sengupta. 1997. "Mid-Crustal Contact Metamorphism Around the Chimakurthy Mafic-Ultramafic Complex, Eastern Ghats Belt, India." *Contributions to Mineralogy and Petrology* 129: 182–197.
- De Andrade, V., O. Vidal, E. Lewin, P. O'Brien, and P. Agard. 2006. "Quantification of Electron Microprobe Compositional Maps of Rock Thin Sections: An Optimized Method and Examples." *Journal of Metamorphic Geology* 24: 655–668.
- De Campos, C. P., S. R. Medeiros, J. C. Mendes, et al. 2016. "Cambro-Ordovician Magmatism in the Araçuaí Belt (SE Brazil): Snapshots From a Post-Collisional Event." *Journal of South American Earth Sciences* 68: 248–268.
- De Capitani, C., and K. Petrakaksi. 2010. "The Computation of Equilibrium Assemblage Diagrams With Theriaik/Domino Software." *American Mineralogist* 95: 1006–1016.
- Degeling, H., S. Eggins, and D. J. Ellis. 2001. "Zr Budgets for Metamorphic Reactions, and the Formation of Zircon From Garnet Breakdown." *Mineralogical Magazine* 65: 749–758.
- Egydio-Silva, M., A. Vauchez, H. Fossen, C. G. G. Cavalcante, and B. C. Xavier. 2018. "Connecting the Araçuaí and Ribeira Belts (SE—Brazil): Progressive Transition From Contractional to Transpressive Strain Regime During the Brasiliano Orogeny." *Journal of South American Earth Sciences* 86: 127–139.
- Ellis, S., C. Beaumont, R. A. Jamieson, and G. Quinlan. 1998. "Continental Collision Including a Weak Zone: The Vise Model and Its Application to the Newfoundland Appalachians." *Canadian Journal of Earth Sciences* 35: 1323–1346.
- Engi, M., P. Lanari, and M. J. Kohn. 2017. "Significant Ages—An Introduction to Petrochronology." *Reviews in Mineralogy and Geochemistry* 83: 1–12.
- England, P. C., and A. B. Thompson. 1984. "Pressure—Temperature—Time Paths of Regional Metamorphism I. Heat Transfer During the Evolution of Regions of Thickened Continental Crust." *Journal of Petrology* 25: 894–928.
- Farias, P., R. F. Weinberg, A. Sola, and M. Finch. 2023. "Protracted Thermal Evolution of a Migmatitic Terrane as Revealed by Multiple Geochronometers From the Retro-Arc of the Early Paleozoic Famatinian Orogen in NW Argentina." *Tectonics* 42: e2021TC007027.
- Fossen, H., C. Cavalcante, and R. P. Almeida. 2017. "Hot Versus Cold Orogenic Behaviour: Comparing the Araçuaí-West Congo and the Caledonian Orogenes." *Tectonics* 36: 2159–2178.
- Fossen, H., C. Cavalcante, J. Konopásek, et al. 2020. "A Critical Discussion of the Subduction-Collision Model for the Neoproterozoic Araçuaí-West Congo Orogen." *Precambrian Research* 343: 105715.
- Fuck, R. A., B. B. Brito-Neves, and C. Schobbenhaus. 2008. "Rodinia Descendentes in South America." *Precambrian Research* 160: 108–126.
- Gradim, C., J. Roncato, A. C. Pedrosa-Soares, et al. 2014. "The Hot Back-Arc Zone of the Araçuaí Orogen, Eastern Brazil: From Sedimentation to Granite Generation." *Brazilian Journal of Geology* 44: 155–180.
- Harley, S. 2016. "A Matter of Time." *Journal of Mineralogical and Petrological Sciences* 111: 50–72.
- Heilbron, M., A. C. Pedrosa-Soares, M. Campos Neto, L. C. Silva, R. A. J. Trouw, and V. C. Janasi. 2004. "A Província Mantiqueira." In *O Desvendar de um Continente: A Moderna Geologia da América do Sul e o Legado da Obra de Fernando Flávio Marques de Almeida*, edited by V. Mantesso-Neto, A. Bartorelli, C. D. R. Carneiro, and B. B. Brito Neves, 203–234. Beca.
- Herman, J., and D. Rubatto. 2003. "Relating Zircon and Monazite Domains to Garnet Growth Zones: Age and Duration of Granulite Facies Metamorphism in the Val Malenco Lower Crust." *Journal of Metamorphic Geology* 21: 833–852.
- Holland, T. J. B., and R. Powell. 1998. "An Internally Consistent Thermodynamic Data Set for Phases of Petrological Interest." *Journal of Metamorphic Geology* 16: 309–343.
- Holland, T. J. B., and R. Powell. 2003. "Activity–Composition Relations for Phases in Petrological Calculations: An Asymmetric Multicomponent Formulation." *Contributions to Mineralogy and Petrology* 145: 492–501.
- Jamieson, R. A., C. Beaumont, S. Medvedev, and M. H. Nguyen. 2004. "Crustal Channel Flows: 2. Numerical Models With Implications for Metamorphism in the Himalayan-Tibetan Orogen." *Journal of Geophysical Research: Solid Earth* 109: B06407.
- Jamieson, R. A., C. Beaumont, C. J. Warren, and M. H. Nguyen. 2010. "Crustal Channel Flows: 2. Numerical Models With Implications for Metamorphism in the Himalayan-Tibetan Orogen." *Canadian Journal of Earth Sciences* 47: 517–539.
- Jiao, S., M. Brown, R. N. Mitchell, et al. 2023. "Mechanisms to Generate Ultrahigh-Temperature Metamorphism." *Nature Reviews Earth and Environment* 4: 298–318.
- Jochum, K. P., U. Weis, B. Stoll, et al. 2011. "Determination of Reference Values for NIST SRM 610–617 Glasses Following ISO Guidelines." *Geostandards and Geoanalytical Research* 35: 397–429.
- Johnson, T., C. Clark, R. J. M. Taylor, M. Santosh, and A. S. Collins. 2015. "Prograde and Retrograde Growth of Monazite in Migmatites: An Example From the Nagercoil Block, Southern India." *Geoscience Frontiers* 6: 373–387.
- Johnson, T. A., J. D. Vervoort, M. J. Ramsey, J. N. Aleinikoff, and S. Southworth. 2018. "Constraints on the Timing and Duration of Orogenic Events by Combined Lu-Hf and Sm-Nd Geochronology: An Example From the Grenville Orogeny." *Earth and Planetary Science Letters* 501: 152–164.
- Johnson, T. A., J. D. Vervoort, M. J. Ramsey, S. Southworth, and S. R. Mulcahy. 2020. "Tectonic Evolution of the Greenville Orogen in the Central Appalachians." *Precambrian Research* 346: 105740.
- Kelly, S., C. Beaumont, and J. P. Butler. 2020. "Inherited Terrane Properties Explain Enigmatic Post-Collisional Himalayan-Tibetan Evolution." *Geology* 48: 8–14.
- Kelly, S., C. Beaumont, and R. Jamieson. 2022. "Eohimalayan Metamorphism and Subsequent Tectonic Quiescence Explained." *Earth and Planetary Science Letters* 584: 117350.
- Lanari, P., and M. Engi. 2017. "Local Bulk Composition Effects on Metamorphic Mineral Assemblages." *Reviews in Mineralogy and Geochemistry* 83: 55–102.
- Lanari, P., O. Vidal, V. De Andrade, et al. 2014. "XMapTools: A MATLAB®-Based Program for Electron Microprobe X-Ray Image Processing and Geothermobarometry." *Computers & Geosciences* 62: 227–240.
- Lanari, P., A. Vho, T. Bovay, L. Airagui, and S. Centrella. 2019. "Quantitative Compositional Mapping of Mineral Phases by Electron Probe Micro-Analyser." *Geological Society, London, Special Publications* 478: 39–63.
- Lugmair, G. W., and K. Marti. 1978. "Lunar Initial $^{142}\text{Nd}/^{144}\text{Nd}$: Differential Evolution of the Lunar Crust and Mantle." *Earth and Planetary Science Letters* 39: 349–357.

- Melo, M. G., G. Stevens, C. Lana, et al. 2017a. "Two Cryptic Anatectic Events Within a Syn-Collisional Granitoid From the Araçuaí Orogen (Southeastern Brazil): Evidence From the Polymetamorphic Carlos Chagas Batholith." *Lithos* 277: 51–71.
- Melo, M. G., L. Lana, G. Stevens, et al. 2017b. "Assessing the Isotopic Evolution of S-Type Granites of the Carlos Chagas Batholith, SE Brazil: Clues From U-Pb, Hf Isotopes, Ti Geothermometry and Trace Element Composition of Zircon." *Lithos* 284–285: 730–750.
- Melo, M. G., C. Lana, G. Stevens, M. E. Hartwig, M. S. Pimenta, and H. A. Nalini Jr. 2020. "Deciphering the Source of Multiple U-Pb Ages and Complex Hf Isotope Composition in Zircon From Post-Collisional Charnockite-Granite Associations From the Araçuaí Orogen (Southeastern Brazil)." *Journal of South American Earth Sciences* 103: 102792.
- Mondou, M., M. Egydio-Silva, A. Vauchez, M. I. B. Raposo, O. Bruguier, and A. F. Oliveira. 2012. "Complex, 3D Strain Patterns in a Synkinematic Tonalite Batholith From the Araçuaí Neoproterozoic Orogen (Eastern Brazil): Evidence From Combined Magnetic and Isotopic Chronology Studies." *Journal of Structural Geology* 39: 158–179.
- Montero, P., F. Bea, T. F. Zinger, J. H. Scarrow, J. F. Molina, and M. Whitehouse. 2004. "55 Million Years of Continuous Anatexis in Central Iberia: Single-Zircon Dating of the Peña Negra Complex." *Journal of the Geological Society* 161: 255–263.
- Moraes, R., C. Nicollet, J. S. F. Barbosa, R. A. Fuck, and A. R. Sampaio. 2015. "Applications and Limitations of Thermobarometry in Migmatites and Granulites Using as an Example Rocks of the Araçuaí Orogen in Southern Bahia, Including a Discussion on the Tectonic Meaning of the Current Results." *Brazilian Journal of Geology* 45: 517–539.
- Munhá, J. M. U., U. G. Cordani, C. C. G. Tassinari, and T. Paácios. 2005. "Petrologia e Termocronologia de Gnaisses Migmatíticos da Faixa de Dobramentos Aracuaí (Espírito Santo, Brasil)." *Revista Brasileira de Geociências* 35: 123–134.
- Parsons, A. J., K. Hosseini, R. M. Palin, and K. Sigloch. 2020. "Geological, Geophysical and Plate Kinematic Constraints for Models of the India-Asia Collision and the Post-Triassic Central Tethys Oceans." *Earth-Science Reviews* 208: 103084.
- Paton, C., J. Hellstrom, B. Paul, J. Woodhead, and J. Herget. 2011. "Iolite: Freeware for the Visualisation and Processing of Mass Spectrometric Data." *Journal of Analytical Atomic Spectrometry* 26: 2508–2518.
- Pearce, N. J. G., W. T. Perkins, J. A. Westgate, et al. 1997. "A Compilation of New and Published Major and Trace Element Data for NIST SRM 610 and NIST SRM 612 Glass Reference Materials." *Geostandards Newsletter* 21: 115–144.
- Pedrosa-Soares, A. C., and C. M. Wiedemann-Leonardos. 2000. "Evolution of the Araçuaí Belt and Its Connection to the Ribeira Belt, Eastern Brazil." In *Tectonic Evolution of South America*, edited by U. G. Cordani, E. Milani, A. Thomaz-Filho, and D. A. Campos, 265–285. Sociedade Brasileira de Geologia.
- Pedrosa-Soares, A. C., P. Vidal, O. H. Leonardos, and B. B. Brito-Neves. 1998. "Neoproterozoic Oceanic Remnants in Eastern Brazil: Further Evidence and Refutation of an Exclusively Ensisalic Evolution for the Araçuaí-West Congo Orogen." *Geology* 26: 519–522.
- Pedrosa-Soares, A. C., C. M. Noce, C. M. Wiedemann, and C. P. Pinto. 2001. "The Araçuaí-West-Congo Orogen in Brazil: An Overview of a Confined Orogen Formed During Gondwanaland Assembly." *Precambrian Research* 110: 307–323.
- Pedrosa-Soares, A. C., C. De Campos, C. M. Noce, et al. 2011. "Late Neoproterozoic–Cambrian Granitic Magmatism in the Araçuaí Orogen (Brazil), the Eastern Brazilian Pegmatite Province and Related Mineral Resources." *Geological Society, London, Special Publications* 350: 25–51.
- Peixoto, E., A. C. Pedrosa-Soares, F. F. Alkmim, and I. A. Dussin. 2015. "A Suture-Related Accretionary Wedge Formed in the Neoproterozoic Araçuaí Orogen (SE Brazil) During Western Gondwanaland Assembly." *Gondwana Research* 27: 878–896.
- Petitgirard, S., A. Vauchez, M. Egydio-Silva, et al. 2009. "Conflicting Structural and Geochronological Data From the Ibituruna Quartz-Syenite (SE Brazil): Effect of Protracted "Hot" Orogeny and Slow Cooling Rate?" *Tectonophysics* 477: 174–196.
- Petrus, J. A., and B. S. Kamber. 2012. "VizualAge: A Novel Approach to Laser Ablation ICP-MS U-Pb Geochronology Data Reduction." *Geostandards and Geoanalytical Research* 36, no. 3: 247–270.
- Richter, F., C. Lana, G. Stevens, et al. 2016. "Sedimentation, Metamorphism and Granite Generation in a Back-Arc Region: Records From the Ediacaran Nova Venecia Complex (Araçuaí Orogen, Southeastern Brazil)." *Precambrian Research* 272: 78–100.
- Rocha, B. C., R. Moraes, A. Möller, C. R. Cioffi, and M. J. Jercinovic. 2017. "Timing of Anatexis and Melt Crystallization in the Socorro-Guaxupé Nappe, SE Brazil: Insights From Trace Element Composition of Zircon, Monazite and Garnet Coupled to U-Pb Geochronology." *Lithos* 277: 337–355.
- Rubato, D. 2017. "Zircon: The Metamorphic Mineral." *Reviews in Mineralogy and Geochemistry* 83: 261–295.
- Rubato, D., J. Hermann, A. Berger, and M. Engi. 2009. "Protracted Fluid-Induced Melting During Barrovian Metamorphism in the Central Alps." *Contributions to Mineralogy and Petrology* 158: 703–722.
- Ryback, L. 1988. "Determination of Heat Production Rate." In *Handbook of Terrestrial Heat Flow Density Determination*, edited by R. Hänel, L. Ryback, and L. Stegna, 125–142. Kluwer Academic Publishers.
- Schannor, M., C. Lana, G. Nicoli, et al. 2021. "Reconstructing the Metamorphic Evolution of the Araçuaí Orogen (SE Brazil) Using In Situ U-Pb Garnet Dating and P-T Modelling." *Journal of Metamorphic Geology* 39: 1145–1171.
- Serrano, P., A. C. Pedrosa-Soares, E. Medeiros-Júnior, et al. 2018. "A-Type Medina Batholith and Post-Collisional Anatexis in the Araçuaí Orogen (Se Brazil)." *Lithos* 320–321: 515–536.
- Shabeer, K. P., K. Sajeev, T. Okudaira, and M. Santosh. 2002. "Two-Stage Spinel Growth in the High-Grade Metapelites of the Central Kerala Khondalite Belt: Implication for Prograde P-T Path." *Journal of Geosciences. Osaka City University* 45: 29–43.
- Smit, M. A., E. E. Scherer, and K. Mezger. 2013. "Lu-Hf and Sm-Nd Garnet Geochronology: Chronometric Closure and Implications for Dating Petrological Processes." *Earth and Planetary Science Letters* 381: 222–233.
- Smit, M. A., J. C. Vrijmoed, E. E. Scherer, et al. 2024. "Retentiveness of Rare Earth Elements in Garnet With Implications for Garnet Lu-Hf Chronology." *Journal of Metamorphic Geology* 42: 703–727.
- Smithies, R. H., H. M. Howard, P. M. Evans, et al. 2011. "High-Temperature Granite Magmatism, Crust-Mantle Interaction and the Mesoproterozoic Intracontinental Evolution of the Musgrave Province, Central Australia." *Journal of Petrology* 52: 931–958.
- Smithies, R. H., C. L. Kirkland, F. J. Korhonen, et al. 2015. "The Mesoproterozoic Thermal Evolution of the Musgrave Province in Central Australia—Plume vs. the Geological Record." *Gondwana Research* 27: 1419–1429.
- Söderlund, U., P. J. Patchett, J. D. Vervoort, and C. E. Isachsen. 2004. "The ^{176}Lu Decay Constant Determined by Lu-Hf and U-Pb Isotope Systematics of Precambrian Mafic Intrusions." *Earth and Planetary Science Letters* 219: 311–324.
- Spear, F. S., M. J. Kohn, and J. T. Cheney. 1999. "P-T Paths From Anatetic Pelites." *Contributions to Mineralogy and Petrology* 134: 17–32.
- Tedeschi, M., T. Novo, A. C. Pedrosa-Soares, et al. 2016. "The Ediacaran Rio Doce Magmatic Arc Revisited (Araçuaí-Ribeira Orogenic System, SE Brazil)." *Journal of South American Earth Sciences* 68: 167–186.

- Temporim, F. A., R. Trindade, M. Egydio-Silva, et al. 2023. "Vertical Deformation Partitioning Across a Collapsing Large and Hot Orogen." *Terra Nova* 35: 23–31.
- Turlin, F., C. Deruy, A. Eglinger, et al. 2018. "A 70 ma Record of Suprasolidus Conditions in the Large, Hot, Long-Duration Grenville Orogen." *Terra Nova* 30: 233–243.
- Van Achterbergh, E., C. G. Ryan, and W. L. Griffin. 2000. "GLITTER: On-Line Interactive Data Reduction for the Laser Ablation ICP-MS Microprobe." In *Cambridge: Ninth Annual VM Goldschmidt Conference, Abstract 7215*.
- Vanderhaeghe, O. 2012. "The Thermal–Mechanical Evolution of Crustal Orogenic Belts at Convergent Plate Boundaries: A Reappraisal of the Orogenic Cycle." *Journal of Geodynamics* 56–57: 124–145.
- Vauchez, A., A. Tommasi, and M. Egydio-Silva. 1994. "Self-Indentation of a Heterogeneous Continental Lithosphere." *Geology* 22: 967–970.
- Vauchez, A., M. Egydio-Silva, M. Babinski, A. Tommasi, A. Uhlein, and D. Liu. 2007. "Deformation of a Pervasively Molten Middle Crust: Insights From the Neoproterozoic Ribeira-Araçuaí Orogen (SE Brazil)." *Terra Nova* 19: 278–286.
- Vauchez, A., M. H. Hollanda, P. Monié, M. Mondou, and M. Egydio-Silva. 2019. "Slow Cooling and Crystallization of the Roots of the Neoproterozoic Araçuaí Hot Orogen (SE Brazil): Implications for Rheology, Strain Distribution, and Deformation Analysis." *Tectonophysics* 766: 500–518.
- Vermeesch, P. 2018. "IsoplotR: A Free and Open Toolbox for Geochronology." *Geoscience Frontiers* 9: 1479–1493.
- Vervoort, J. D., P. J. Patchett, U. Söderlund, and M. Baker. 2004. "Isotopic Composition of Yb and the Determination of Lu Concentrations and Lu/Hf Ratios by Isotope Dilution Using MC-ICPMS." *Geochemistry, Geophysics, Geosystems* 5: Q1102.
- White, R. W., R. Powell, and G. L. Clarke. 2002. "The Interpretation of Reaction Textures in Fe-Rich Metapelitic Granulites of the Musgrave Block, Central Australia: Constraints From Mineral Equilibria Calculations in the System." *Jurnal of Metamorphic Geology* 20: 41–55.
- White, R. W., N. E. Pomroy, and R. Powell. 2005. "An In Situ Metatexite–Diatexite Transition in Upper Amphibolite Facies Rocks From Broken Hill, Australia." *Jurnal of Metamorphic Geology* 23: 579–602.
- White, R. W., R. Powell, and T. J. B. Holland. 2007. "Progress Relating to Calculation of Partial Melting Equilibria for Metapelites." *Jurnal of Metamorphic Geology* 25: 511–527.
- Whitney, D. L., and B. W. Evans. 2010. "Abbreviations for Names of Rock-Forming Minerals." *American Mineralogist* 95: 185–187.
- Wiedenbeck, M., P. Allé, F. Corfu, et al. 1995. "Three Natural Zircon Standards for U–Th–Pb, Lu–Hf, Trace Element and REE Analyses." *Geostandards Newsletter* 19: 1–23.
- Wisnioski, L., A. C. Pedrosa-Soares, E. Medeiros-Junior, J. Belém, I. Dussin, and G. Queiroga. 2020. "Ultra-High Temperature, Mid-Crustal Level, Contact Metamorphism Imprinted on Granulite Facies Paragneisses by a Norite Intrusion (São Gabriel da Baunilha, Araçuaí Orogen, Southeast Brazil)." *Jurnal of Metamorphic Geology* 39: 867–895.
- Yakymchuk, C. 2023. "Prograde Zircon Growth in Migmatites." *Jurnal of Metamorphic Geology* 41: 719–743.

Supporting Information

Additional supporting information can be found online in the Supporting Information section. **Data S1:** X-Ray maps parameters. **Data S2:** T-X phase diagrams. **Data S3:** Support petrographic features. **Data S4:** Mineral chemistry data - ARAC-01. **Data S5:** Mineral chemistry data - ARAC-02. **Data S6:** Mineral chemistry data - ARAC-03. **Data S7:** Geochronology and REEs data. **Data S8:** P-T-t data compilation and heat rates.